Reconstruction de la surface de Fermi par ordre de densité de charge dans le supraconducteur cuprate LSCO

par

Seyedeh Arezoo Ahmadi Afshar

Mémoire présenté au département de physique
en vue de l'obtention du grade de maître ès sciences (M.Sc.)

FACULTÉ des SCIENCES
UNIVERSITÉ de SHERBROOKE

Sherbrooke, Québec, Canada, 25 juin 2018

Le 25 juin 2018

le jury a accepté le mémoire de Madame Seyedeh Arezoo Ahmadi Afshar dans sa version finale.

Membres du jury

Professeur Louis Taillefer
Directeur de recherche
Département de physique

Professeur Bertrand Reulet
Président rapporteur
Département de physique

Professeur Glen Evenbly
Deuxième membre
Département de physique

À K1

Abstract

Since the discovery of cuprate superconductors in 1986, the key enduring question is: why is the superconducting transition temperature T_c so high? An answer to this question requires that we understand the link between the superconducting phase and two other phases of cuprates: a phase of charge-density-wave (CDW) order and the mysterious pseudogap phase. We also need to understand the link between the latter two phases.

For my MSc project, my goal was to delineate the region of CDW order in the doping phase diagram of the cuprate $La_{2-x}Sr_xCuO_4$ (LSCO), in the $T = 0$ limit in the absence of superconductivity. For this purpose, I performed measurements of the Hall coefficient R_H and the Seebeck coefficient S at low temperature and high magnetic field, on several samples of LSCO in the doping range from $x = 0.07$ to $x = 0.15$. Because the magnetic field needed to suppress superconductivity at some of these dopings exceeds 20 T, some measurements had to be done at high magnetic field laboratories, namely the Laboratoire National des Champs Magéntique Intenses in Grenoble and the National High Magnetic Field Laboratory in Tallahassee. Transport measurements can detect the presence of CDW order via the impact that it has on the Fermi surface, namely a reconstruction that produces a small electron-like Fermi pocket, detected as a drop in $R_H(T)$ and S/T to negative values at low temperature, as previously established for the cuprate YBCO [1, 2, 3]. In LSCO, we observe a similar drop in $R_H(T)$ and S/T to negative values at $x = 0.11$, 0.12 and 0.13, the three dopings where CDW order has been observed by x-ray diffraction [4]. Extending to lower and higher dopings, we find that CDW-induced Fermi-surface reconstruction is confined to $0.085 < p < 0.15$. The fact that the CDW phase ends at $p_{CDW} = 0.15$, distinctly below the end point of the pseudogap phase at $p^* = 0.18$, implies that the two phases are distinct. One can therefore treat them separately in their impact on superconductivity.

Résumé

Depuis la découverte des cuprates supraconducteurs en 1986, la plus importante question qui demeure est : pourquoi leur température de transition supraconductrice T_c est-elle si élevée? Obtenir une réponse à cette question requiert que l'on comprenne le lien entre la phase supraconductrice et deux autres phases des cuprates : une phase d'onde de densité de charge (ODC) et la mystérieuse phase pseudogap. Il est aussi important de comprendre le lien entre ces deux dernières phases.

Lors de mon projet de maîtrise, mon but était de délimiter la région dans laquelle l'ODC subsiste dans le diagramme de phase du cuprate $La_{2-x}Sr_xCuO_4$ (LSCO) dans la limite $T = 0$ en l'absence de la supraconductivité. À cette fin, j'ai effectué des mesures des coefficients de Hall R_H et Seebeck S à basse température et à champ magnétique intense sur différents échantillons de LSCO dans un intervalle de dopage entre $x = 0.07$ et $x = 0.15$. Puisque le champ magnétique requis pour supprimer la supraconductivité à certains de ces dopages excède 20 T, certaines mesures ont dû être effectuées dans des laboratoires de champs magnétiques intenses, spécifiquement au Laboratoire National des Champs Magnétiques Intenses à Grenoble et au National High Magnetic Field Laboratory à Tallahassee. Les mesures de transport peuvent détecter la présence d'ODC via l'effet que cet ordre a sur la surface de Fermi, notamment une reconstruction qui produit une petite poche d'électrons, détectable par une chute de $R_H(T)$ et de S/T vers des valeurs négatives à basse température tel qu'établi dans le cuprate YBCO [1, 2, 3]. Dans LSCO, nous observons un chute similaire de $R_H(T)$ et de S/T vers des valeurs négatives à $x = 0.11, 0.12$ et 0.13, les trois dopages auxquels l'ODC a été observée par diffraction des rayons X [4]. En étendant l'étude à des dopages plus bas et plus élevés, nous trouvons que la reconstruction de la surface de Fermi induite par l'ODC est confinée à $0.085 < p < 0.15$. Le fait que l'ODC disparaisse à $p_{CDW} = 0.15$, bien en dessous du point limite de la phase pseudogap à $p^* = 0.18$, implique que ces deux phases sont distinctes. Elles peuvent donc être traitées séparément lorsqu'on étudie leur impact sur la supraconductivité.

Acknowledgment

I would first like to thank my thesis advisor Prof. Louis Taillefer. He kindly steered me in the right the direction whenever he thought I needed it. Thank you for giving the opportunity to be in your amazing group.

I very much appreciate to Nicolas. The door of Nicolas's office was always open whenever I ran into a trouble spot or had a question about my research. I would also thanks to Sven for letting me know how to run the experiment. He helped me learn what I needed to do my research. Also, Thanks to Simon. You taught me how to be careful, patient, and thoughtful before and while performing the experiment. I would also like to acknowledge Adrien and Patrick as the second readers of this thesis, and I am gratefully indebted to them for their very valuable comments on this thesis.

I must express my very profound gratitude to my family and to my husband, Keyvan for providing me with unfailing support and continuous encouragement throughout my years of study and through the process of researching and writing this thesis. This accomplishment would not have been possible without them. Thank you!

And finally, thank you with tears in my eyes to my dear uncle Jacques who taught me how to be strong and to be happy. I really miss you Jacques.

Contents

List of Tables

List of Figures

Introduction

Cuprate high-T_c superconductors were discovered more than three decades ago but the mechanism which is responsible for superconductivity in these materials has not yet been clearly established. The temperature versus doping phase diagram of cuprates contains many different phases and ordered states. At low doping, the parent compounds are Mott insulators with antiferromagnetic order. At very high doping, they become metals with Fermi liquid behavior. In between, the superconducting state develops as a dome. On the left side of the superconducting dome, there is a mysterious phase which is called pseudogap at high temperature. Coexisting with superconductivity are charge density wave and spin density wave orders — periodic modulations of the density of charge or spin within the material.

The obvious and fundamental question is : Why is the critical temperature so high in cuprates? Some other important open questions are : Why does superconductivity appear as a dome? What is the impact of other phases on the superconducting state?
The key to solving these puzzles could be in understanding the mechanism of the pseudogap phase. There are some possibilities whether the pseudogap connects to charge density wave or it could be a high temperature precursor of the charge density wave.

The goal of my project was to investigate the possible connection between pseudogap and charge density wave so we needed to pin down the charge density wave region. In the phase diagram, it is already known from YBCO that the charge density wave reconstructs the Fermi surface [2]. In this project, I used Seebeck and Hall measurements to characterize the Fermi surface reconstruction and thereby determine the region in which there is charge density wave order in the cuprate LSCO [1].

Chapter 1 of this report gives a brief history of cuprate superconductors and the signature of Fermi surface reconstruction in cuprates. Chapter 2 presents the theoretical and

[1] $La_{2-x}Sr_xCuO_4$

experimental aspects of the two measurements used to probe the Fermi surface reconstruction: the Hall effect and the Seebeck effect. Finally, the high magnetic field measurements of Hall coefficient and Seebeck coefficient in LSCO are presented and discussed in chapter 3.

Chapter 1

Cuprate superconductors

Cuprate superconductors are copper oxide based materials and they were the first high-T_c unconventional superconductors to be discovered. By changing doping (hole / electron concentration) in cuprates, different ground states will appear and these produce a very rich phase diagram.
In this chapter, I mainly focus on the general phase diagram of cuprates and then I explain how different orders reconstruct the Fermi surface.

1.1 Cuprate high-T_c superconductors

Mercury was the first superconductor to be discovered by Kamerlingh Onnes in 1911. He observed that the electrical resistivity of a mercury wire suddenly disappeared when it was cooled below a temperature of about 4 K. This exciting discovery in low temperature physics earned him the Nobel Prize in 1913. Finding materials that remain superconducting up to room temperature would pave the way for superconductors to be used in daily life and for their application to be widespread. For example, they would eliminate power loss in transmission lines and could provide more affordable forms of magnetic levitation transit systems. Therefore, people are working to find materials that are superconductors at room temperature. Figure 1.1 shows the maximum critical temperature of superconductors as a function of their year of discovery. From 1973 to 1986, people believed that Nb_3Ge had the highest reachable $T_c \simeq 24$ K. In 1986, Bednorz and Müller opened a new horizon in superconductivity with the discovery of LBCO [1] with $T_c = 30$ K [5]. Only one year later, $YBa_2Cu_3O_{7-x}$ was discovered with a maximum $T_c = 92$ K [6], higher than the boiling point

[1] $La_{2-x}Ba_xCuO_4$

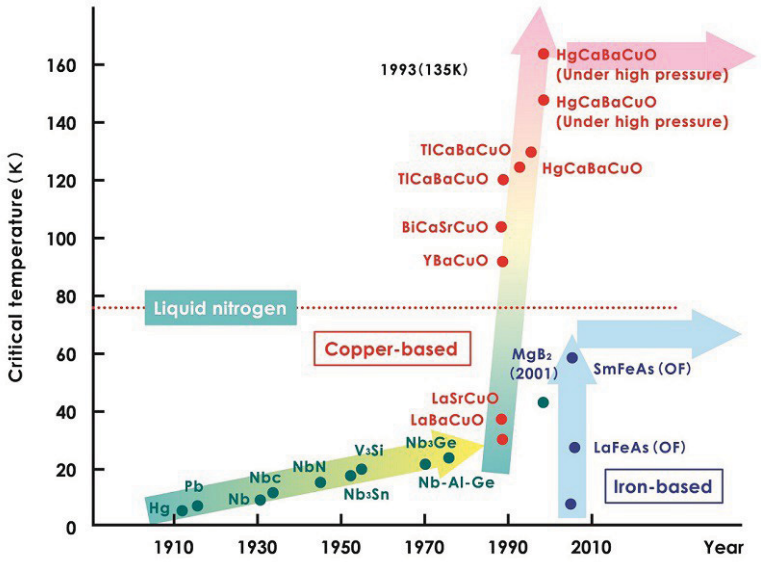

Figure 1.1 Superconducting transition temperature vs. year of discovery since mercury as the first superconductor in 1911. https://thiscondensedlife.wordpress.com/2016/08/14/drought/

of liquid nitrogen ($T \simeq 77$ K). This new generation of high-T_c superconductors is called ***cuprates*** and it developed rapidly, a material with T_c higher than half of room temperature was discovered soon after [7]. However, the current record for the highest critical temperature belongs to hydrogen sulfide (H_2S) which has a T_c of 203 K when an extremely high pressure of 150 GPa is applied [8].

1.1.1 Crystal structure

Cuprates have a perovskite crystal structure. Figure 1.2 shows the typical crystal structure of cuprates. They consist of two types of layers; *copper oxide conductive planes* which control the physics of high T_c superconductivity, and *insulating charge reservoirs* which are located between the CuO_2 planes and may dope electrons or holes into the CuO_2 planes. Figure 1.3 shows the crystal structure of LSCO, which is a single layer hole doped cuprate superconductor with $T_c^{max} = 38$ K. Between the neighboring CuO_2 planes in LSCO, there are two layers of La(Sr)-O planes. The lattice constants of LSCO in the orthorhombic phase are $a \simeq 5.35$ $\dot{A}$, $b \simeq 5.40$ $\dot{A}$ and $c \simeq 13.15$ $\dot{A}$, however the exact value of a, b and c depend on the doping. By increasing the doping, the difference between a and b disappears as the material approaches a tetragonal structure, so that beyond $x \simeq 0.22$ the tetragonal phase persists to $T = 0$. The lattice constants in the tetragonal phase of LSCO are $a = b \simeq 3.812$ $\dot{A}$. One of

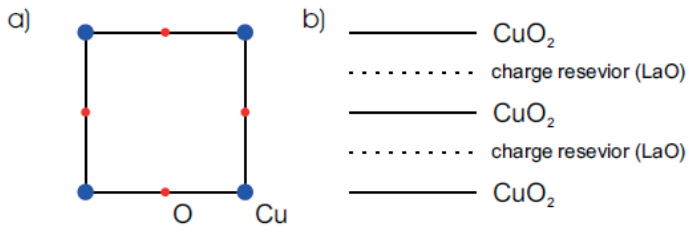

Figure 1.2 The crystal structure of cuprates has two main features; **(a)** The conductive CuO_2 plane. **(b)** The alternative layering of conductive planes and insulating charge layers along the c-axis [9].

the main tuning parameters in cuprates is doping. In fact, tuning the doping p leads to the appearance of different ground states. In hole doped systems, when electrons are removed from the charge reservoir layers, the doping p changes in the copper oxide planes. In LSCO, the parent compound of which is La_2CuO_4, there is one hole per Cu atom because the valence state of Cu is $3d^9$. The substitution of Sr^{+2} on the La^{+3} site introduces one additional hole in the CuO_2 plane. In the material $La_{2-x}Sr_xCuO_4$, x represents the doping value of the hole concentration in the CuO_2 planes *i.e*, $x = p$. In the next session, I present the generic phase diagram of cuprates and the different phases that compose it.

1.1.2 Phase diagram

Figure 1.4 shows the generic temperature (T) as a function of hole concentration (p) phase diagram of cuprates. Several states develop in the phase diagram of cuprates which we outline here.

antiferromagnetic Mott insulator (AF)

In cuprates, at zero doping (parent compound), there is an insulating phase with a half filled orbital which is called the Mott insulator. Below a certain temperature, called the Néel temperature (T_N), the spins of the copper atoms have an antiferromagnetic order in which the spins alternate from up to down from site to site to minimize the energy of the system [11]. Doping suppress the antiferromagnic order rapidly. For example in La_2CuO_4 with $T_N \simeq 325$ K [12], antiferromagnetic order completely disappears by substituting 2% of La^{2+} atoms by Sr^{3+}.

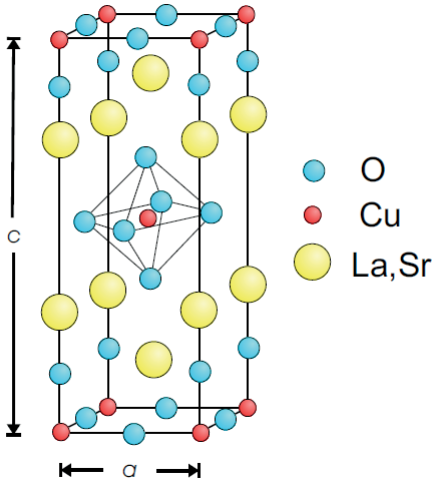

Figure 1.3 Body centered tetragonal structure of LSCO. A copper oxide plane is located in the center of the structure with La, Sr atoms on the other side along *c*-axis [9].

Fermi Liquid (FL)

At high doping, the material becomes a Fermi liquid metal where the resistivity is proportional to T^2 [13].
There are several electronic states between the Mott insulator at low doping and the Fermi liquid at high doping. These states can be accessed by hole doping the parent compound and are described below.

Spin density wave (SDW)

Spin density wave (SDW) order is a state of mater with a periodic modulation of the spin density. The new periodicity of SDW in LSCO samples has been observed by neutron scattering [14, 15, 16, 17, 18], nuclear magnetic resonance (NMR) and muon spin resonance (μSR) [19].

Charge density wave (CDW)

Charge density wave (CDW) order is a modulation of the conduction electron density in a metal and an associated modulation of the lattice atomic positions. Figure 1.5 shows x-ray diffraction intensity from CDW modulations in $YBa_2Cu_3O_{6.67}$ with $T_c = 67$ K at different magnetic field $H = 0$, 7.5, 15 and 17 T [20].
Incommensurate CDW [1] is observed below $T_{CDW} \approx 135$ K inside of pseudogap state. Below

[1] Incommensurate CDW means the CDW wavelength is not an integer multiple of the lattice constant.

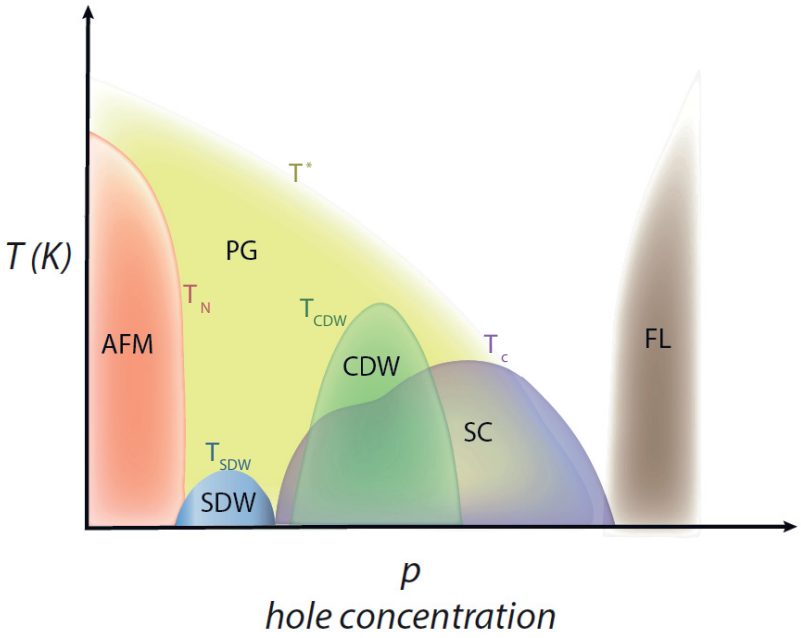

Figure 1.4 The general temperature T vs. doping p phase diagram of hole-doped cuprates. The schematic shows the doping dependence of antiferromagnetic (AF) transition temperature T_N, spin density wave order (SDW) transition temperature T_{SDW}, superconducting (SC) transition temperature T_c, charge density wave order (CDW) transition temperature T_{CDW} and pseudogap crossover temperature T^*, Fermi liquid (FL) region is also showed at high doping [10].

T_{CDW}, the intensity of CDW order keeps increasing at $H = 0$ T until the material enters the superconducting state. Below T_c, the intensity of CDW starts decreasing. When a high magnetic field is applied, enough to suppress superconductivity, the intensity of CDW continually increases down to low temperature while the onset temperature of CDW does not change. These two observations strongly suggest that there is a competition between CDW and superconductivity [20].

Pseudogap (PG)

The pseudogap (PG) phase is manifested by a partial loss of electronic states at low energy below a crossover temperature T^*. Figure 1.6 shows the NMR Knight shift in $Bi_2Sr_{1.6}La_{0.4}CuO_{6+\delta}$ vs. temperature T at different magnetic fields [21].

The Knight shift essentially measures the spin susceptibility which is directly proportional to the density of states (DOS). The Knight shift curve is flat at high temperature as expected for metals but it deviates and monotonically decreases below T^*. This downturn is

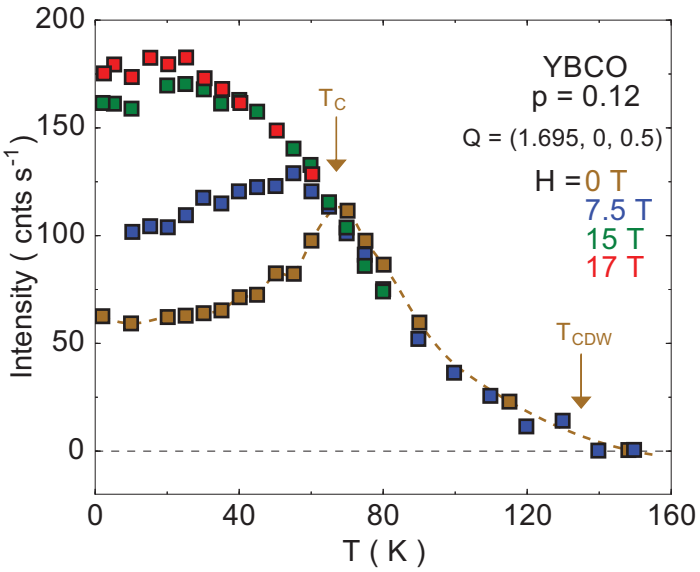

Figure 1.5 Temperature dependence of the x-ray diffraction intensity from CDW order in YBCO at $p = 0.12$ in $H = 0$, 7.5, 15 and 17 T [20].

independent of magnitude of the magnetic field. The reduction in Knight shift indicates a loss of DOS, which means a gap opens below T^*, well above T_c. Understanding the mechanism of the PG phase has been a major challenge and it is not clear whether it is an ordered phase or a fluctuation regime.

Superconductivity

The superconducting state appears as a dome at intermediate doping where the transition temperature T_c is the temperature where the resistance reaches zero and the Meissner effect [1] is observed. Optimal doping is the doping at which is the maximal critical temperature. It divides the superconducting dome into two regions: 1) a region where T_c increases with an increase in doping which is called the underdoped region and 2) a region where T_c decreases with increasing doping which is called the overdoped region. Figure 1.7 shows the superconducting dome in LSCO. Superconductivity emerges at doping $x = 0.05$ and reaches its maximum T_c of 38 K at a doping $x \simeq 0.15$ [22].

An anomaly in T_c is observed on the underdoped side of superconducting dome. In the case of LSCO, a dip is observed around a doping of $p = 1/8$ [22]. This dip in the superconducting dome probably comes from the competition between CDW and superconductivity because the CDW is maximum at $p = 1/8$ and it might be competition between stripe order [2] and

[1] The Meinssner effect is the expulsion of a magnetic field from a superconductor.
[2] A combination of charge-density-wave (CDW) and spin-density-wave (SDW) modulations.

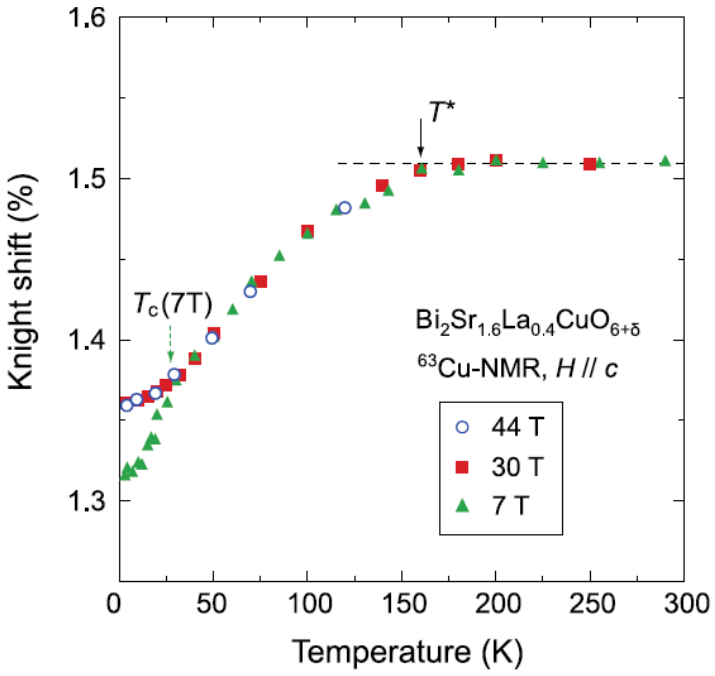

Figure 1.6 NMR Knight shift in $Bi_2Sr_{1.6}La_{0.4}CuO_{6+\delta}$ vs. temperature T at various magnetic fields. The Knight shift curve is flat at high temperature but below T^*, it starts dropping which means a gap opens in the DOS below T^* hence the name "pseudogap" [21].

superconducting state.

1.2 Evolution of the Fermi surface in cuprates

In order to characterize and predict the thermal, electrical, magnetic, and optical properties of materials, knowledge of the Fermi surface is particularly important. In this section, I discuss the evolution of the Fermi surface as well the phase diagram of cuprates.

1.2.1 Fermi surface in overdoped regime

Figure 1.8 shows the different Fermi surfaces of cuprates at various dopings and temperatures.

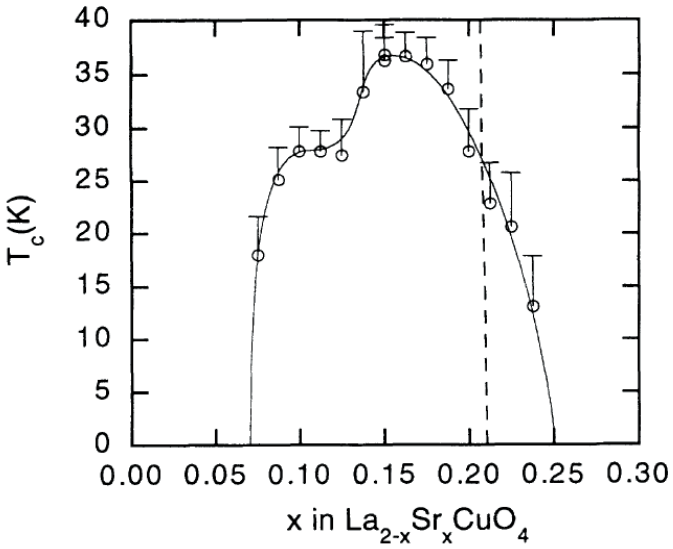

Figure 1.7 The superconducting transition T_c in LSCO as a function of doping p, the circle data is obtained via the magnetic susceptibility. The solid line a guid to the eye [22].

On the overdoped side of the phase diagram, Platé *et al.* measured the Fermi surface of Tl-2201 [1] at very high doping ($p = 0.30$) with ARPES [2]. They showed that the Fermi surface consists of a single large hole-like cylinder centered at (π, π) (Figure 1.8(a)) [23]. In the same material and for the same doping, at low temperature, Vignolle *et al.* observed quantum oscillations [3] with a very high frequency $F = 18100$ T (Figure 1.8(b)) [24].
As stated by the Onsager relation $F = \frac{\hbar}{2\pi e} A_F$ (frequency of the quantum oscillations F is directly proportional to the Fermi surface area A_F), the Fermi surface area is $A_F = 172.8$ nm^2, some 65 % of the first Brillouin zone.
Figure 1.9 shows the transformation of the Fermi surface as seen by the Hall effect for various dopings of YBCO [27]. Figure 1.9 (a) shows the Hall coefficient R_H of overdoped YBCO ($p \geq 0.16$). For YBCO at a doping $p = 0.205$, a standard positive Hall effect with a small amplitude is observed (yellow curve) and this is in agreement with what is expected for a large Fermi surface.
Doping dependence of the Hall number n_H is shown in Figure 1.10 for hole-doped cuprates. n_H is given by V/eR_H where V is the volume, e is the electron carrier and R_H corresponds to Hall coefficient. The Hall number of Tl-2201 (open diamond) at high doping ($p \simeq 0.27$) is

[1] $Tl_2Ba_2CuO_{6+\delta}$
[2] Angle-Resolved Photoemission Spectroscopy
[3] When an external magnetic field is applied, quasiparticles start performing cyclotron orbits which are quantized as Landau level. Quantum oscillations occurs when the magnetic field increases and Landau levels cross the Fermi surface which causes the density of states at the Fermi level to oscillate.

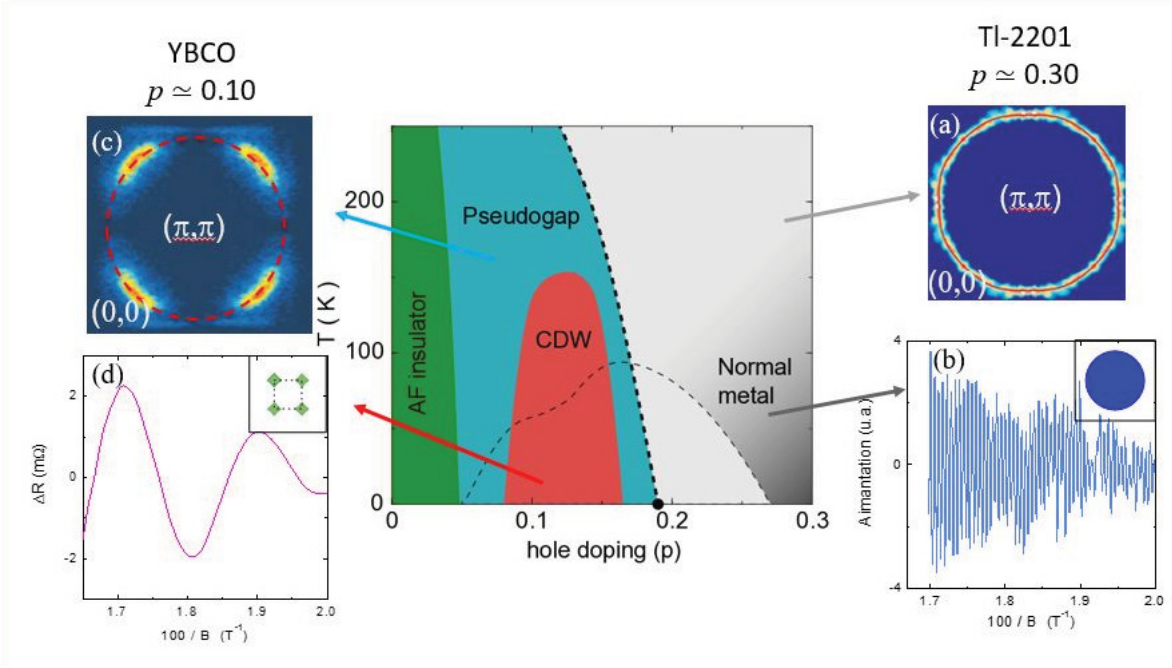

Figure 1.8 (a) ARPES measurements show that the Fermi surface of overdoped Tl-2201 at a doping $p = 0.30$ is a large hole-like cylinder centered at (π , π)[23] (b) High frequency $F = 18100$ T quantum oscillations are observed at the same doping [24], (c) At hight T, in the pseudogap phase Fermi arcs appear in ARPES measurement of underdoped YBCO at a doping $p = 0.10$ [25] while (d) at low temperature, the Fermi arcs transform into small Fermi pockets as seen by the detection of quantum oscillations with slow frequency $F = 530$ T in the CDW phase[26].

$n_H = 1 + p$ [28]. This is also the case in Nd-LSCO [1] at $p = 0.24$ [29].

1.2.2 Fermi surface in pseudogap phase

On the underdoped side, Hossain *et al.* measured ARPES of YBCO [2] at a doping $p = 0.10$. Figure 1.8 (c) shows Fermi arcs at the antinode $(\pi/2,\pi/2)$. Fermi arcs are the signature of the pseudogap phase in YBCO on the underdoped side of the phase diagram[25]. For YBCO at a doping $p = 0.10$ and at low temperature, quantum oscillations with very small frequency $F = 530$ T were observed [26]. The corresponding Fermi surface area is $A_F = 5.1$ nm^2, which represents only 1.9 % of the first Brillouin zone. These quantum oscillations with slow frequency indicate there is a small and closed Fermi surface, however Fermi arcs

[1] $La_{1.6-x}Nd_{0.4}Sr_xCuO_4$
[2] $YBa_2Cu_3O_y$

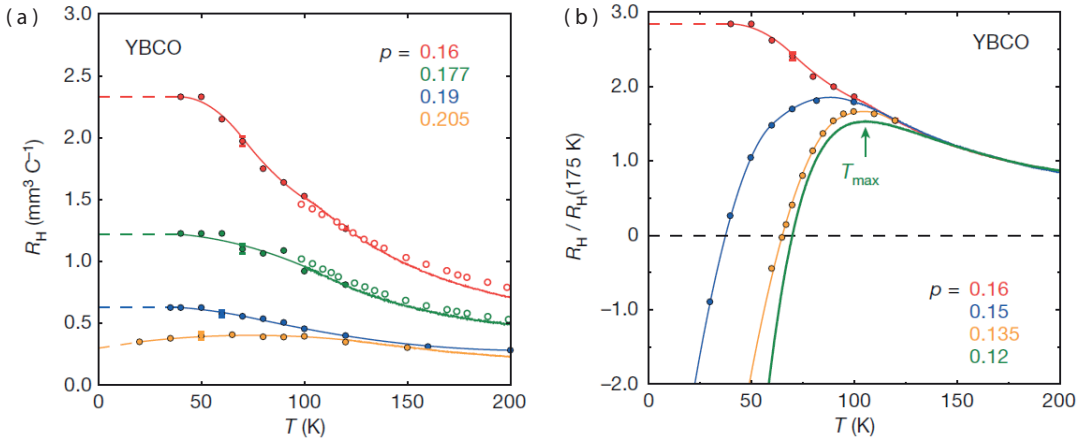

Figure 1.9 The normal-state Hall coefficient R_H as a function of temperature T for YBCO (a) A doping $p = 0.205$ R_H has a positive and small value in agreement with large Fermi surface. Below the critical point of the pseudogap at a doping $p^* = 0.19$, R_H increases when the temperature decreases [27, 31]. (b) A dopings $p = 0.15, 0.135$ and 0.12 R_H drops at T_{max} and then becomes negative [27].

were observed at high temperature. In underdoped Hg-1201 cuprate [1] at a doping $p = 0.09$, the observed quantum oscillations with small frequency reveal a similar Fermi surface as underdoped YBCO [30].

At a doping $p^* = 0.19$, where we cross the end point of the pseudogap phase, R_H dramatically increases. But in Figure 1.9 (b) for underdoped YBCO, below a critical doping $p = 0.16$ (red curve) something else happens with Hall coefficient. At dopings $p = 0.12$, 0.125 and 0.15, R_H is still positive at high temperature then at T_{max}, it suddenly drops and keeps decreasing with decreasing temperature insofar as it finally becomes negative for lower temperatures. This negative Hall coefficient in YBCO is not alone, Seebeck also shows negative value and it is not limited to YBCO. In following section, I discuss the negative Hall and Seebeck coefficients.

In Figure 1.10, we see a sharp drop in the Hall number when the pseudogap opens at p^*, from $n_H = 1 + p$ at high doping to $n_H = p$ at low doping and it is also observed in Nd-LSCO [29]. This rapid loss of carrier density is the transport signature of the pseudogap phase [27] [32].

[1] $HgBa_2CuO_{4+\delta}$

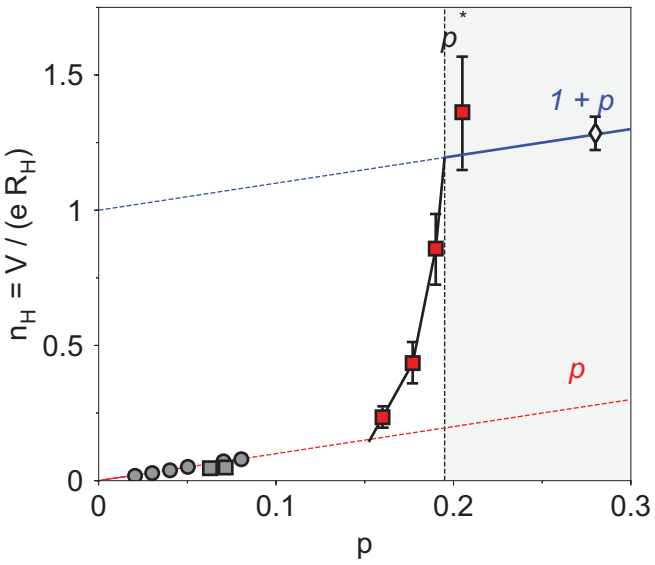

Figure 1.10 Doping dependence of the Hall number n_H in hole doped cuprates. The open diamond is for overdoped Tl-2201 in the $T = 0$ limit of $R_H(T)$ [28]. The red squares are for YBCO at $p > 0.15$ and the gray squares are for YBCO at $p < 0.08$ [27, 31]. The gray circles is the Hall number of LSCO [32]. The red line is $n_H = p$, the blue line is $n_H = 1 + p$ and the black line is a guide to the eyes [27].

1.2.3 Electron pockets in the Fermi surface

By studying quantum oscillations, we can determine the size of the closed Fermi surface. However, we cannot determine if the Fermi surface is electron-like or hole-like. The sign of carriers present on the Fermi surface is identified by performing transport measurements of the Hall and Seebeck coefficients.

Negative Hall coefficient

In a simple Drude model, the electrical Hall coefficient is defined:

$$R_H = \pm \frac{V}{en} \tag{1.1}$$

n is the carrier density, V is the unit cell volume, e the elementary charge of the electron, and the minus (plus) sign corresponds to electrons (holes). Figure 1.11 shows the Hall coefficient as a function of temperature in YBCO at a doping $p = 0.10$ [1] and in Hg1201 at a doping $p = 0.12$ [33] in the presence of a magnetic field high enough to reach the normal state. YBCO and Hg1201, both have positive Hall coefficients at high temperature, which drop when the

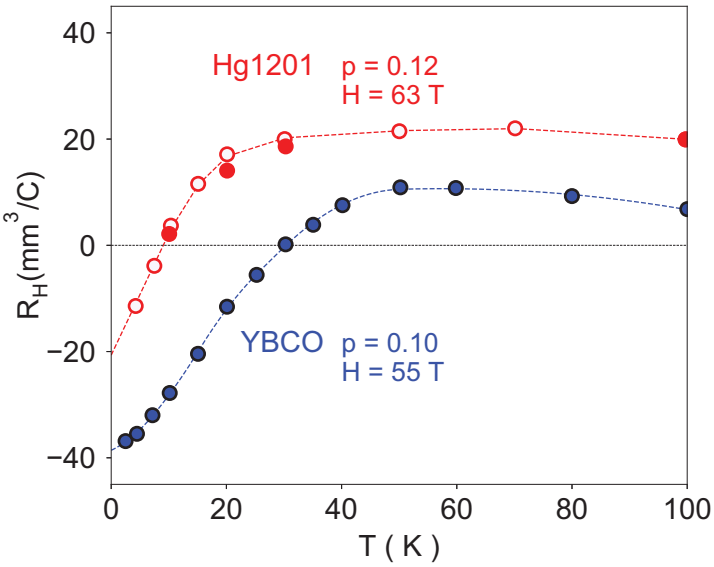

Figure 1.11 Hall coefficient R_H versus temperature T for YBCO at doping $p = 0.10$ (blue circles) at $H+$ 55 T [1] and Hg1201 at doping $p = 0.12$ (red circles) with magnetic field $H = 53$ T (close red circles) and 63 T (open red circles) [33].

temperature decreases and eventually become negative at low temperature. The positive Hall coefficient at high temperature indicates the the dominant carriers on the Fermi surface are holes but they change to electrons when the Hall coefficient becomes negative at low temperature. As Figure 1.12 shows, the measured Hall coefficients in Nd-LSCO [34], LBCO [1] [35] and LSCO [36] show behaviors similar to R_H in YBCO and Hg1201.

The combination of a negative Hall coefficient and a small Fermi surface at low temperature which is extracted from quantum oscillations, allows us to conclude that the Fermi surface of YBCO and Hg-1201 is reconstructed from a large hole Fermi surface at high temperature to a Fermi surface consisting mainly of small electron pockets at low temperature.

Negative Seebeck coefficient

In addition to the Hall effect, the Seebeck coefficient S is also sensitive to the type of carriers on the Fermi surface. Figure 1.13 shows the Seebeck coefficient S/T versus temperature for YBCO at a doping $p = 0.10$ and for Hg1201 at a doping $p = 0.12$ in a high magnetic field in order to reach the normal state [2]. For both cuprates, S/T is positive at high temperature and it becomes negative by decreasing the temperature. Similar sign changes in S/T are

[1] $La_{2-x}\ Ba_x\ CuO_{4+\delta}$

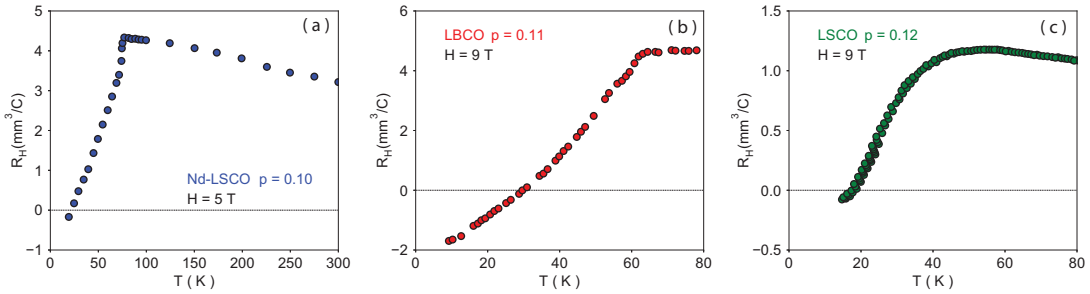

Figure 1.12 Hall coefficient R_H as a function of temperature T for (a) Nd-LSCO $p = 0.10$ at $H = 5$ T [34] (b) LBCO $p = 0.11$ at $H = 9$ T [35] (c) LSCO $p = 0.12$ at $H = 9$ T [36]. In all three cuprates the Hall coefficient R_H becomes negative at low temperature.

also observed in Eu-LSCO [1] [2]. As we have already seen in the Hall effect, a positive and a negative value of S/T represents hole and electron carriers respectively.

The magnitude of the Seebeck coefficient at $T \to 0$ is given by [37]:

$$S/T \approx \pm(\pi^2/3)(3/2+\zeta)(k_B/e)\frac{1}{T_F}. \tag{1.2}$$

where e and k_B are the electron charge and the Boltzman constant respectively. ζ depends on energy dependence of the relaxation: $\zeta = 0$ corresponds to an energy-independent relaxation time and $\zeta = 1/2$ corresponds to typical energy dependence. The Fermi temperature T_F can be calculated from the quantum oscillation frequency and is given by :

$$T_F = (\frac{e\hbar}{k_B})\frac{F}{m^*}.$$

Where F is the frequency and m^* is the effective mass. In YBCO $p = 0.11$, $T_F = 410 \pm 20$ K (quantum oscillations gives F =520 T and $m^* = 1.76 \pm 0.07\ m_0$ (m_0 is the electron mass) [38] are calculated), from Equation 1.2, we obtain $S/T = -\ 0.9 \pm 0.2\ \mu\text{VK}^{-2}$ where the negative sign is for electron-like Fermi surface. The measured value at low temperature is $S/T = -\ 0.8 \pm 0.1\ \mu\text{VK}^{-2}$ [2] which agrees very well with the theoretical value. Note that this is a single-band calculation and may not work for multi-band systems.

[1] $La_{1.8-x}Eu_{0.2}Sr_xCuO_4$

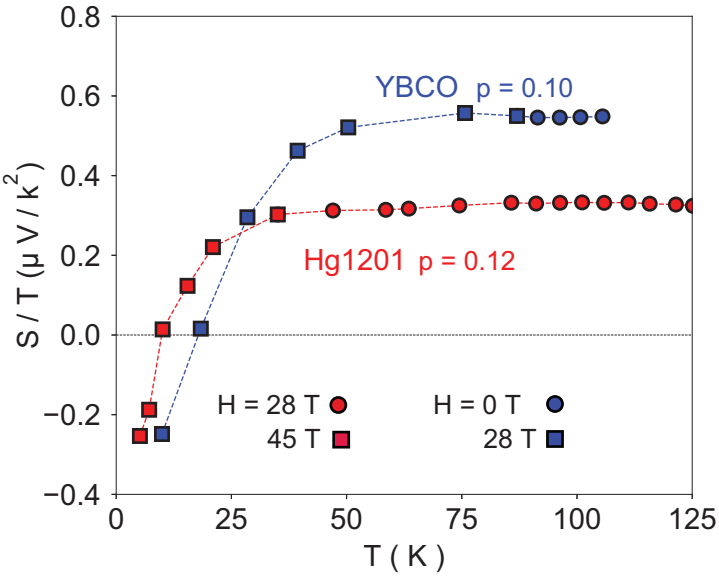

Figure 1.13 The Seebeck coefficient as a function of temperature is lotted as S/T vs T in the normal state for magnetic fields $H = 0$ T (blue circles) and $H = 28$ T (blue squares) in YBCO at a doping $p = 0.10$ and also $H = 28$ T (red circles) and $H = 45$ T (red squares) on Hg1201 at a doping $p = 0.12$ [2].

1.3 Fermi surface reconstruction

1.3.1 Fermi surface reconstruction by AF order

So far, we have studied the Fermi surface in cuprates. On the overdoped side, whether at high or at low temperatures, the Fermi surface is a **large hole cylinder**. In contrast, on the underdoped side, the Fermi surface has an **arc** shape at high temperatures below p^*, while it reconstructs to **small electron pockets** at low temperatures. So on the underdoped side, the Fermi surface undergoes a reconstruction when temperature decreases. This transformation is due to a new periodicity of the electronic system that reduces the Brillouin zone and folds any part of the Fermi surface that intersects the new zone boundary.

Figure 1.14 shows an example of this phenomena, for an antiferromagnetic (AF) commensurate order with a (π, π) wave vector. This wave vector changes the Brillouin zone from a square to a diamond and the folding of the Fermi surface causes the appearance of hole pockets a $(\pm\frac{\pi}{2}, \pm\frac{\pi}{2})$ and electron pockets a $(\pm\pi, 0)$ and $(0. \pm\pi)$. This kind of transformation explains how small electron-like pockets can appear out of a large hole-like Fermi surface.

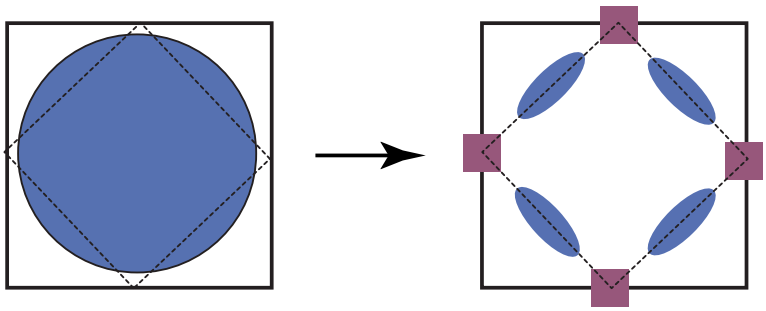

Figure 1.14 Sketch of how (left) the large hole Fermi surface (blue) that exists in the overdoped region of the cuprate phase diagram would be reconstructed by antiferromagnetic order (right) into small hole (blue) and electron (red) pockets [39].

1.3.2 Fermi surface reconstruction by charge order

Fermi arcs are seen in the pseudogap phase by ARPES [25], but by cooling down, the Fermi surface is reconstructed to small electron pockets [1, 2] [26]. A question raises; what happens to the pseudogap when temperature drops? For Eu-LSCO, X-ray diffraction detects stripe order in same doping range in which Fermi surface reconstruction is observed through the sign change in the Seebeck coefficient [2]. Therefore we conclude that Fermi surface reconstruction coexists with stripe order in Eu-LSCO.

The red curve in Figure 1.15 shows the temperature dependence of the Hall coefficient for YBCO at a doping $p = 0.12$ with an applied magnetic field $H = 15$ T [1]. T_H is the inflexion point of R_H where it starts turning down. T_{max} is the temperature where R_H has its maximum value before it drops and becomes negative. The charge order is also observed by x-ray diffraction in YBCO at the same doping and field (blue dots) [20]. We see that the onset temperature of CDW modulation T_{CDW} coincides roughly with T_H indicating that charge order is likely responsible for the Fermi surface reconstruction.

Figure 1.16 shows the phase diagram of YBCO, temperature versus doping. The green triangles (up and down) is taken from x-ray diffraction measurement and shows the range of doping where CDW is observed , below T_{CDW} [3][41]. T_H and T_S correspond to the temperatures where the Hall coefficient $R_H(T)$ and Seebeck coefficient $S(T)$ become negative respectively. The doping region under T_H and T_S, where Fermi surface reconstruction is observed, covers exactly the doping region where there is CDW order. Therefore the Fermi surface reconstruction matches with the region of CDW as a function of doping. The results

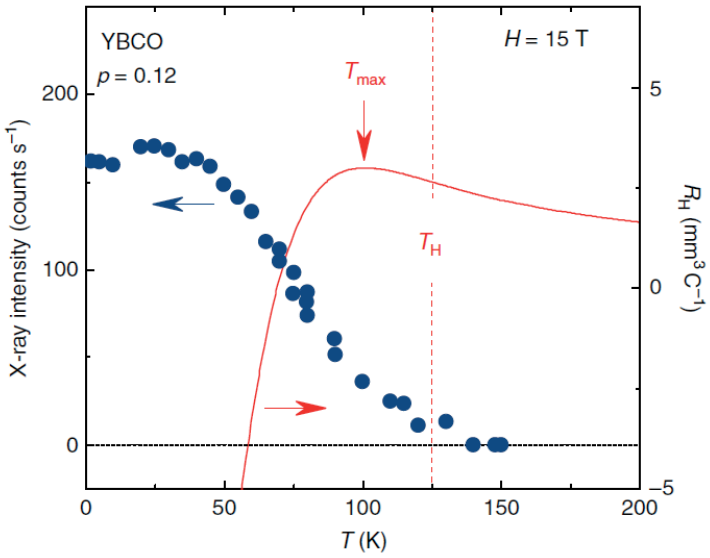

Figure 1.15 Hall coefficient of YBCO as a function of temperature at a doping p =0.12 (T_c =66 K), at H =15 T [1]. The evolution of R_H(T) is compared with the growth of charge-density-wave modulations detected by X-ray diffraction, at the same doping and field[20] [40].

from Figures 1.15 and 1.16 strongly suggest that Fermi surface reconstruction from Fermi arcs to small electron pockets is caused by CDW in YBCO. A possible scenario for the Fermi surface reconstruction into electron-like pockets by charge order is illustrated in Figure 1.17. Cuprates start with a large hole like Fermi surface at high doping. Then in the pseudogap phase, gaps are opened and the Fermi surface gets cut into Fermi arcs. By cooling down the charge order modulations appears, the arcs fold via wavevectors $\mathbf{Q}_a$ and $\mathbf{Q}_b$, producing to an electron-like pocket [42].

X-ray diffraction on LSCO reveals a similar behavior to YBCO. Figure 1.18 (a) shows the CDW intensity at three different dopings $x = 0.11$, 0.12 and 0.13 in zero magnetic field. Incommensurate CDW is observed in all three samples below a temperature $T_{CDW} = 51$ K, 75 K and 80 K respectively. It is in competition with superconductivity [4].
In Figure 1.18 (b), we plot T_{CDW} versus p in LSCO (green triangles) and also indicates the pseudogap critical point at doping $p^* \simeq 0.18$ (red triangle) [43] . A central question is the relation between the PG and CDW, and whether they are actually the same. To investigate this issue, I determined the doping range where CDW can be observed and pinned down the end point of CDW at low temperature. The connection between FSR and CDW modulation motivated us to use the Seebeck and Hall coefficients in LSCO as a way to detect CDW. For

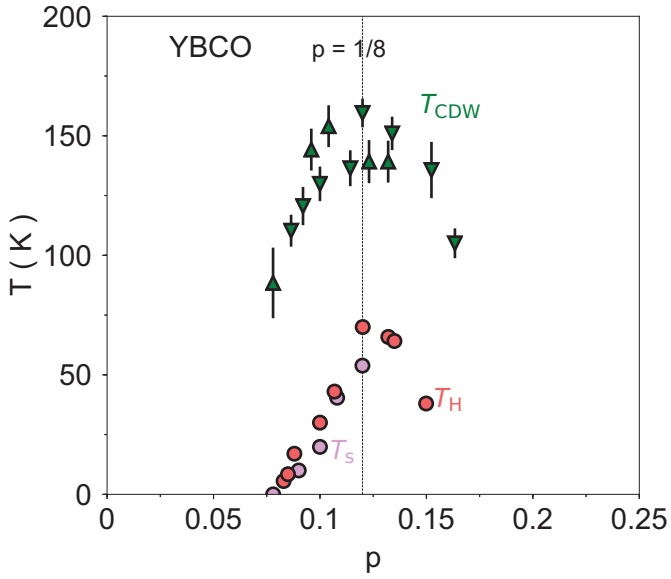

Figure 1.16 Temperature - doping phase diagram shows T_H (red circles) where the Hall coefficient $R_H(T)$ becomes negative [1], T_s (pink circles) where the Seebeck coefficient S/T becomes negative [2] and T_{CDW} (up and down triangles) is the onset temperature of charge density wave order that is detected by X-ray diffraction [3][41].

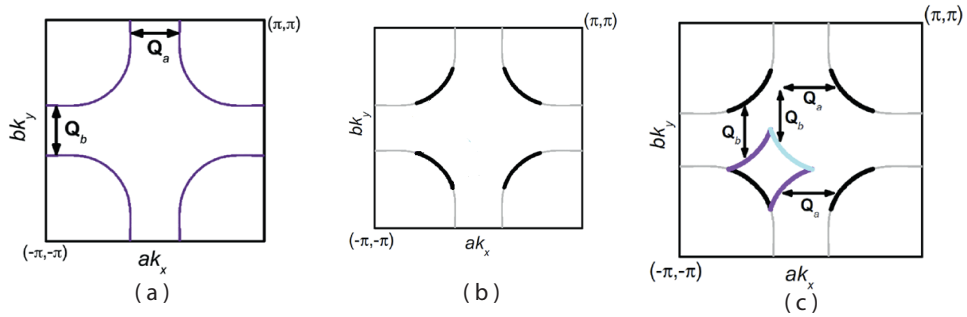

Figure 1.17 The proposed Fermi surface reconstruction caused by biaxial charge order via a two step transformation. (a) Large hole- like Fermi surface of the overdoped cuprates [23] (b) It get cuts into Fermi arcs in the pseudogap phase [25] and finally, (c) where CDW order appears at low temperature, the Fermi arcs fold with $\mathbf{Q}_a$ and $\mathbf{Q}_b$ wavevectors, producing a small closed diamond-shaped electron pocket [42].

this purpose a high magnetic field is required to suppress superconductivity and reach CDW state.

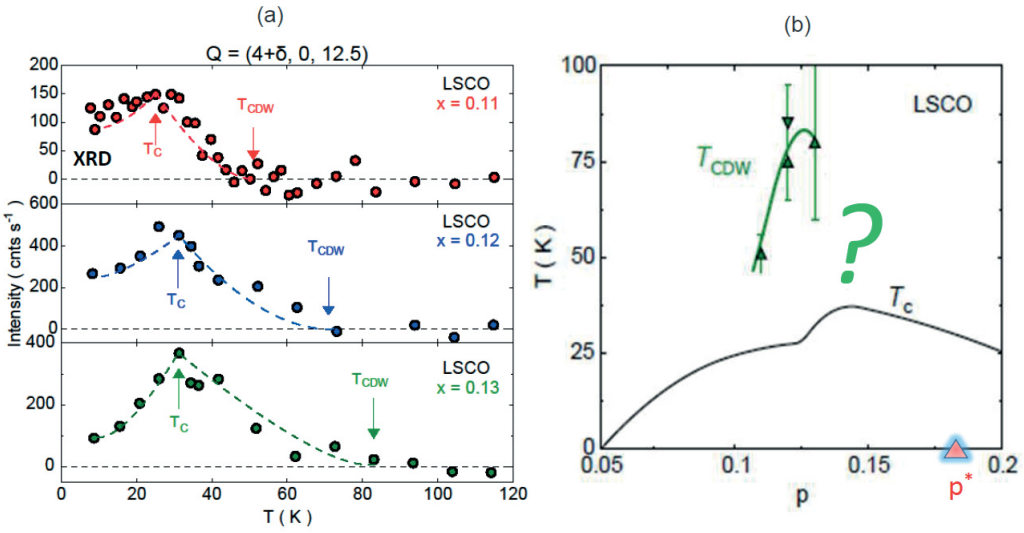

Figure 1.18 (a)Temperature dependence of the peak intensity of the (4 + δ,0,12.5) CDW peak in LSCO for Sr dopings $x = 0.11$,0.12, and 0.13. The dashed line is a guide to the eye. The CDW order decreases below T_c since the material enters the competing superconducting state. [4] [44], (b) Corresponding T_{CDW}, the onset temperature of CDW order, and the end point of the pseudogap at doping $p^* \simeq 0.18$ are shown in the $T - p$ phase diagram of LSCO.

Chapter 2

Transport properties

As shown in chapter 1, the negative values of the Hall and Seebeck coefficients are the signatures of the Fermi surface reconstruction. In this project, we need to reach the normal state at low temperature because we want to pin down the CDW at $T \to 0$. This goal is achievable if the Hall and Seebeck coefficients are measured at strong magnetic field, with superconducting and resistive magnets. This chapter is dedicated to describing the transport properties, namely the Hall and Seebeck effects from theoretical and experimental points of view.

2.1 Theoretical aspects

2.1.1 Hall coefficient R_H

Figure 2.1 shows a sketch of electrical resistivity and Hall effect measurements. The resistivity measurement is explained in Appendix C. In Hall coefficient measurements, an electrical current is typically applied along the x direction such that $\mathbf{J} = J_x\,\hat{\mathbf{e}}_x$ with $J_x = nev$ where e is the electron's charge, n is the density of carriers and v is the velocity of the quasiparticles. Now, if a perpendicular magnetic field $\mathbf{H} = H_z\,\hat{\mathbf{e}}_z$ is applied, the charges are deviated by the Lorentz force:

$$\boldsymbol{F}_L = e(\boldsymbol{E}_H + \boldsymbol{v} \times \boldsymbol{H}). \tag{2.1}$$

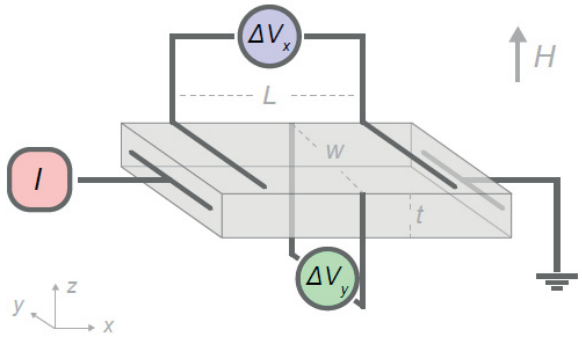

Figure 2.1 Sketch of the transport measurement; electrical resistivity and Hall effect. An electrical current I is applied along the x-axis. This generates a longitudinal potential difference ΔV_x and, when a perpendicular magnetic field H is applied, a transverse potential difference ΔV_y. L, w and t are the sample's dimensions (length, width and thickness, respectively) [45].

Deviated charges accumulate on one side of the sample and this generates an electric field $\mathbf{E}_H = E_y\,\hat{\mathbf{e}}_z$ with $E_y = \Delta V_y t$ where ΔV_y is the transverse voltage and t is the thickness of the sample. In equilibrium, the Lorentz force becomes $\mathbf{F}_L = 0$:

$$e\boldsymbol{E}_H + e(\boldsymbol{v} \times \boldsymbol{H}) = 0. \tag{2.2}$$

As a result we will have:

$$\frac{1}{ne} = \frac{\Delta V_y t}{J_x}\frac{1}{H}. \tag{2.3}$$

So the Hall coefficient is defined as:

$$R_H = \frac{1}{ne}. \tag{2.4}$$

Therefore, in a single band model, at low temperature, the Hall coefficient is a direct measurement of the carrier density n and of the type of carriers.

2.1.2 Seebeck coefficient S

The Seebeck effect is a thermoelectric phenomenon whereby a longitudinal voltage ΔV_x appears in response to the application of a thermal gradient $\Delta T_x = T^+ - T^-$ (Figure 2.2). The

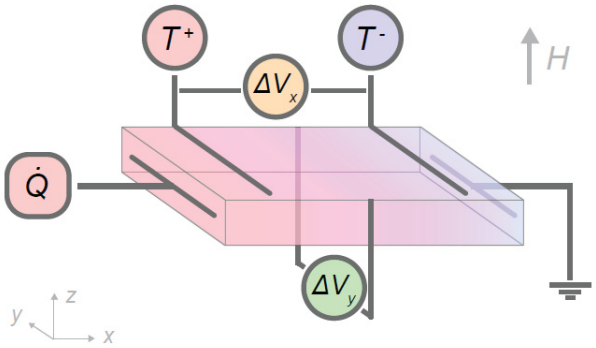

Figure 2.2 Sketch of the Seebeck and Nernst thermoelectric measurements; A heat current $\dot{Q}$ is applied along the x-axis. This generates longitudinal temperature (ΔT_x) and voltage (ΔV_x) differences and, when a perpendicular magnetic field H is applied, a transverse voltage difference ΔV_y [45].

electrical current density (J^e) related to ΔV and ΔT is given by:

$$\boldsymbol{J}^e = -\sigma \boldsymbol{\nabla} V - \alpha \boldsymbol{\nabla} T. \tag{2.5}$$

where $\boldsymbol{\nabla} V$ is a potential gradient, $\boldsymbol{\nabla} T$ is a temperature gradient, σ and α are electric conductivity and Peltier coefficient tensor respectively. In two dimensions, equation 2.5 is written as follows:

$$\begin{bmatrix} J_x \\ J_y \end{bmatrix} = \begin{bmatrix} \sigma_{xx} & \sigma_{xy} \\ \sigma_{yx} & \sigma_{yy} \end{bmatrix} \begin{bmatrix} E_x \\ E_y \end{bmatrix} - \begin{bmatrix} \alpha_{xx} & \alpha_{xy} \\ \alpha_{yx} & \alpha_{yy} \end{bmatrix} \begin{bmatrix} \partial_x T \\ \partial_y T \end{bmatrix}. \tag{2.6}$$

At equilibrium , the electrical current density disappears and the temperature gradient gives rise to a potential difference between the two ends of the sample. So in the absence of charge current density, J_x and J_y are zero and, due to experimental conditions, we only have a temperature gradient along the x direction, so that $\partial_y T = 0$:

$$\sigma_{xx} E_x + \sigma_{xy} E_y - \alpha_{xx} \partial_x T = 0 \tag{2.7}$$

and,

$$\sigma_{yx}E_x + \sigma_{yy}E_y - \alpha_{yx}\partial_x T = 0. \tag{2.8}$$

By extracting E_y from (A.5) and substituting it into (2.7) we have:

$$\sigma_{xx}E_x + \sigma_{xy}\frac{\alpha_{yx}}{\sigma_{yy}} - \sigma_{xy}\frac{\sigma_{yx}}{\sigma_{yy}}E_x\alpha_{xx}\partial_x T = 0. \tag{2.9}$$

The Onsager relations are valid for time reversal symmetry so $\sigma_{yx} = -\sigma_{xy}$ and due to the symmetry of an tetragonal system $\sigma_{xx} = \sigma_{yy}$. The Seebeck coefficient is then:

$$S \equiv \frac{E_x}{\partial_x T} = \frac{\alpha_{xx}\sigma_{xx} + \alpha_{xy}\sigma_{xy}}{\sigma_{xx}^2 + \sigma_{xy}^2}. \tag{2.10}$$

The solution of the Boltzmann equation at low temperature gives the relation between the electric and thermoelectric tensors [46]:

$$\alpha_{ij} = -\frac{\pi^2}{3}\frac{k_B^2 T}{e}\frac{\partial\sigma_{ij}(\epsilon)}{\partial\epsilon}\,|_{\epsilon=\epsilon_F}\,. \tag{2.11}$$

By combining (A.9) and (A.10) and taking $\epsilon = \epsilon_F$ at low temperature we get:

$$S \approx \frac{\alpha_{xx}}{\sigma_{xx}} = \pm\frac{\pi^2 k_B^2 T}{3e}.\frac{1}{\epsilon_F} \tag{2.12}$$

where $\epsilon_F = k_B T_F$. We notice that the thermoelectric power is linear in temperature. It is usual to consider $\frac{S}{T}$, which is non-zero at $T = 0$ and inversely proportional to the Fermi energy.

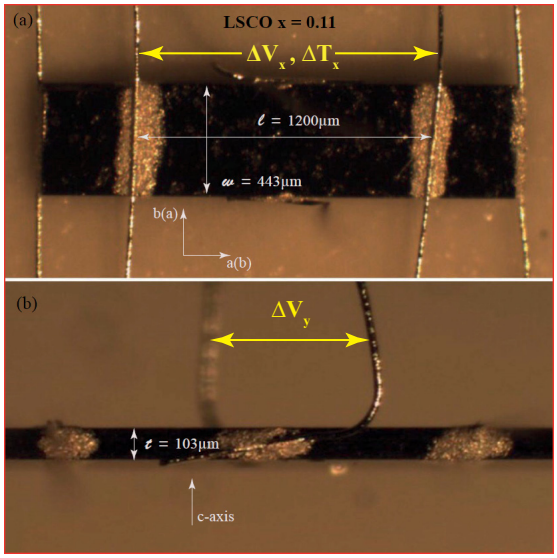

Figure 2.3 Electrical contact on sample LSCO $p = 0.11$ **(a)** There are two pairs of longitudinal contacts : one to apply currents (electrical or thermal) and one to measure ΔV_x and ΔT_x, **(b)** A transverse pair of contacts is glued on opposite edges of the sample to measure ΔV_y.

2.2 Experimental aspects

In this section, I explain the details of how to perform Hall and Seebeck measurements mainly in terms of electrical contacts, instrumentation and data analysis.

2.2.1 Contacts and cryogenics

Contacts

As explained in section 2.1, we need to measure ΔV_y for Hall measurements and $\nabla_x T$ and ΔV_x for Seebeck measurements, so making the electrical contacts is the first step to prepare the sample.

Figure 2.3 shows an LSCO sample at doping $p = 0.11$ with contacts. One pair of longitudinal contacts is connected to the end of the sample (along x) for applying electrical or thermal currents. Two longitudinal contacts, separated by a distance l ($\sim$ mm), are connected to the top face of the sample to measure ΔV_x and ΔT_x. A transverse pair of contacts is connected on the thickness t (~ 100 μm) of the sample with edge a separation w ($\sim$ mm) in order to measure ΔV_y.

The contacts are made with 25 or 50 μm diameter silver wires and they are connected to

the samples, using 2-part Epotech H20E. The sample is then annealed in order to diffuse the epoxy inside the sample slightly. For example, LSCO single crystals should be in a furnace at 500°C in the presence of an oxygen flow for 1 hr.

We make sure that the contacts are correctly made by checking the value of the contacts resistance. If their resistances is less than 5 Ω, it means the contacts are well prepared.

Cryogenic system

Variable temperature insert (VTI)

The variable temperature insert or VTI, as its name implies, is a system that can be used to vary the temperature continuously over a wide range from 1.5 K to 300 K. The VTI is used inside a ^{4}He cryostat and operates by drawing liquid helium through a needle valve which controls the helium flow rate. Then the liquid ^{4}He evaporates when it passes through a heat exchanger (to go below 4.2 K, the VTI fills with liquid helium) into the sample space and is then pumped away by a room temperature vacuum pump. An integral heater and sensor on the heat exchanger allows the temperature to be set to any value between 1.5 to 300 K. All ranges of temperatures are controlled by an Oxford Instrument ITC temperature controller. Temperatures above 4.2 K are obtained by making a balance between the flow of the helium liquid and the heater. Temperatures below 4.2 K, down to 1.5K, are reached by reducing the pressure of helium gas in the sample space.

The superconducting magnet

The highest reachable magnetic field in Sherbrooke is 20 T which is applied by a superconducting magnet. A superconducting magnet is made of coils of superconducting wires. Based on Faraday's law, when a current is applied to the coil, a magnetic field is generated . In the case of a superconducting magnet, the generated magnetic field is much more affordable because below the critical temperature the superconducting wires can conduct a large electrical current without any power loss , because the resistance is zero. Current needed to generate 20 T is 176 A.

The resistive magnet

In order to access higher magnetic fields, we used the DC resistive magnets at the Laboratoire National des Champs Magnétiques Intenses (LNCMI) in Grenoble. The resistive magnet is usually made of copper sheets in the form of a coil. Many holes are added to the coil in order to allow a flow of water to go through it for cooling purposes. The magnetic field can go up to 35 T in the resistive magnet.

The hybrid magnet

In order to go to even higher magnetic fields, one can use a hybrid magnet. The hybrid magnet of the National High Magnetic Field Laboratory (NHMFL) in Tallahassee produces the highest DC magnetic field in the world 45 T. This magnet is a combination of two magnets. There is a superconducting magnet with a 10 T magnetic field on the outside and, on the inside, a resistive magnet which can produce magnetic fields up to 35 T giving a total field of 45 T.

2.2.2 Hall effect

In transport measurements, we need to establish a connection between the sample and the instruments in order to take Hall and Seebeck data in a wide range of temperatures and magnetic fields.

The Hall coefficient data in this project was mainly measured in a PPMS [1] in Sherbrooke which consists of a cryostat with a superconducting magnet coil. In the PPMS, the magnetic field is able to reach $\pm$ 16 T and the available temperature range is 1.9 - 400 K. Figure 2.4 (a) shows the puck used for the measurement of electrical transport in the PPMS. Figure 2.4 (b) is the sketch of sample on the puck for a Hall coefficient measurement. We glue the sample on a sapphire plate to prevent any electrical connection between sample and puck. For Hall measurements, we apply an electrical current along the length of the sample and a magnetic field perpendicular to the sample surface. The transverse voltage V_y gives the transverse resistance R_{xy} by Ohm's law. The Hall voltage being antisymmetrical with magnetic field, we repeat the measurement with the field in the opposite direction to remove any contamination of the signal coming from the misalignment of the Hall contacts. The Hall voltage is therefore given by antisymmetrizing the data :

$$R_{xy} = (R(H) - R(-H))/2. \tag{2.13}$$

Finally, the Hall coefficient R_H is obtained :

$$R_H = R_{xy}\frac{t}{H}. \tag{2.14}$$

where t is the thickness of the sample and R_H is in units of mm^3/C.

For the resistivity in field, we proceed in the same way, but it is symmetrical in field so

[1] Physical Property Measurement System by Quantum Design

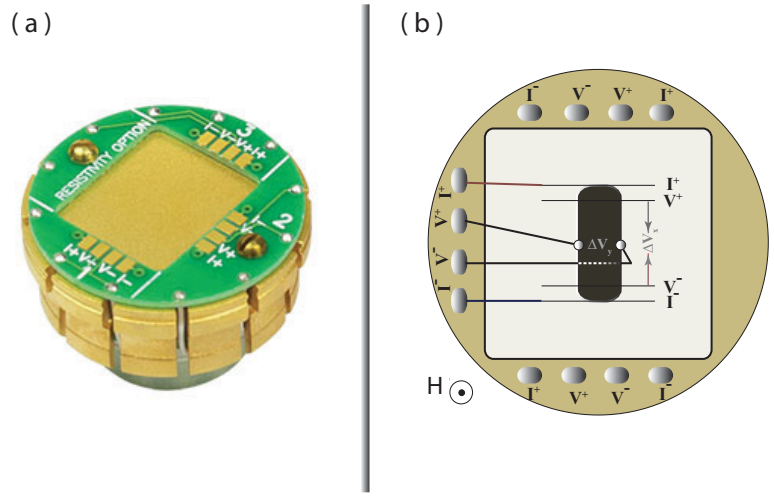

Figure 2.4 (a) The puck which is used in the PPMS for measuring electrical transport namely resistivity and Hall effect. The puck consists of three channels and it allows to measure three physical properties at the same time. http://education.qdusa.com/products.html (b) For a Hall coefficient measurement, the electrical current is applied from I^+ to I^- then a magnetic field H is applied perpendicularly and a transverse voltage ΔV_y is produced.

we symmetrize the data :

$$R_{xx} = (R(H) + R(-H))/2. \tag{2.15}$$

2.2.3 Seebeck effect

Figure 2.5 shows the sample holder which I used for Seebeck measurements. The sample holder is made of copper because of its high thermal conductivity. It is a standard setup with a strain gauge as a heater (because its resistance is independent of temperature and magnetic field), a differential thermocouple to measure the temperature gradient and Phosphor-Bronze wires to measure the Seebeck voltage. These elements are suspended by 10 μm diameter Kevlar wires. The Kevlar wires are used because of their electrically insulating nature and their high tensile strength. All the metal wires (thermocouples, Phosphor-Bronze and strain gauge current) are wound into coils, in order to have a high thermal resistance to avoid heat leaks.

To ensure that the only heat sink for the sample is the copper block it is attached to, we have to seal the sample holder and put it under high vacuum. To do that we use a turbo pump to obtain a 10^{-6} mbar vacuum in the sample space.

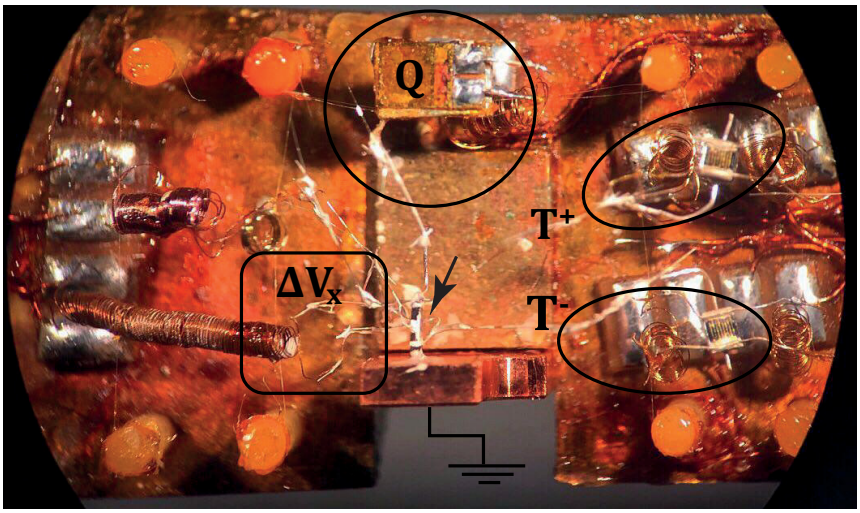

Figure 2.5 The experimental setup used to measure the Seebeck effect. The heater to create $\dot{Q}$, the Seebeck and Nernst coils to take ΔV_x and ΔV_y data respectively and two cernox for measuring T^+ and T^-. The black arrows shows the sample that connects to the copper block.

A calibrated thermometer (Cernox X72820) and a 50 Ω heater are used to regulate the temperature of the probe (T_0) from 5 K to 300 K. The measurement and the regulation of temperature are done by a Lakeshore 340AC resistance bridge.
Silver paint is used to fix one end of the sample to a copper block which is firmly screwed to the sample holder. The copper block plays the role of a thermal ground. A 25 μm silver wire connects the other side of the sample to the strain gauge used to apply the heat current ($\dot{Q}$) generated through Joule heating with an electrical current from a KEITHLEY 6220 current source. The strain gauge is connected to the sample holder by manganin coils because the manganin wire minimizes heat leaks. Phosphor-bronze wires are used to measure the Seebeck voltage because of their low Seebeck coefficient which minimizes contamination of the signal. The longitudinal and transverse voltages are amplified by a factor of 10^3 by NV DC A10 amplifiers and measured with KEITHLEY 2182A nanovoltmeters.

Since we have to apply heat to the sample to create the temperature gradient, the sample temperature increases above the known temperature of the probe. We need to know what the actual temperature of the sample is, so we use an absolute thermocouple to determine the average temperature T_{av}. In the following I will describe how we determine the temperatures with thermocouples and then I will show another method that can be used, where the temperature gradient is measured by thermometers.

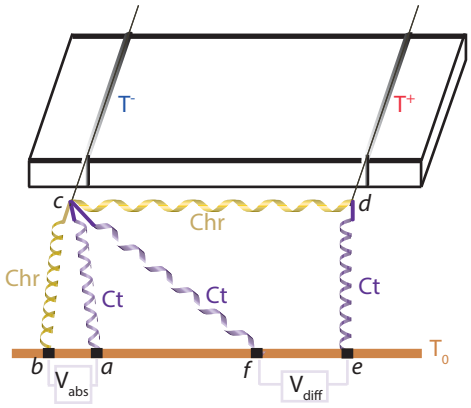

Figure 2.6 Schematic of absolute and differential thermocouples made by chromel (Chr) and constantan (Ct) that measure V_{abs} and V_{diff} respectively.

Thermocouple method

Thermocouples are one of the most widely used temperature sensors to measure ΔT and T_{av} at high temperature.
A thermocouple is made of two different conducting wires. The wires are connected with a spot-weld on one end, their other ends being at a reference temperature. When the junction of the two wires is heated, the temperature gradient between the junction and the reference temperature creates a voltage by Seebeck effect (the temperature dependence of the Seebeck coefficient is very well known).

Figure 2.6 shows a schematic view of a sample with an absolute and a differential thermocouple. Type E (chromel–constantan) thermocouple were used for our experiment because it has a high output (68 μV/°C), which makes it well suited to cryogenic use [47] and it is not non-magnetic so it can be used in high magnetic field [48]. As figure 2.6 shows, the absolute thermocouple measures T^{-}. The voltage is given by:

$$V_{ab} + V_{bc} + V_{ca} = 0. \tag{2.16}$$

By considering the Seebeck equation $V = \int_{T_1}^{T_2} S dT$ and $V_{ab} = V_{abs}$, the equation 2.16 can be written as :

$$V_{abs} = -\int_{T_b}^{T_c} S_{Chr} dT - \int_{T_c}^{T_a} S_{Ct} dT. \tag{2.17}$$

The points a and b of the thermocouple are on the probe so T_a and T_b are equal to T_0 and T_c

is equal to T^- :

$$V_{abs} = -\int_{T_0}^{T^-} S_{Chr}dT + \int_{T_0}^{T^-} S_{Ct}dT = \int_{T_0}^{T^-} (S_{Ct} - S_{Chr})dT.$$

We approximate T_0 and T^- to be very close to each other so we consider that the Seebeck coefficient is constant on this scale so we get :

$$V_{abs} \simeq (S_{Ct} - S_{Ct})(T^- - T_0). \tag{2.18}$$

By measuring V_{abs} and since we know T_0 we can extract the value of T^- with the absolute thermocouple. The temperature gradient is given by measuring the voltage of the differential thermocouple :

$$V_{ef} = -V_{fc} - V_{cd} - V_{de} \tag{2.19}$$

Where the $V_{ef} = V_{diff}$. We can extend the equation 2.19 like we did for absolute thermocouple :

$$V_{diff} = -\int_{T_f}^{T_c} S_{Ct}dT - \int_{T_c}^{T_d} S_{Chr}dT - \int_{T_d}^{T_e} S_{Ct}dT.$$

We have $T_e = T_f = T_0$, $T_c = T^-$ and $T_d = T^+$, so :

$$V_{diff} = -\int_{T_0}^{T^-} S_{Ct}dT - \int_{T^-}^{T^+} S_{Chr}dT - \int_{T^+}^{T_0} S_{Ct}dT$$

$$= \int_{T^-}^{T^+} S_{Ct}dT - \int_{T^-}^{T^+} S_{Chr}dT$$

$$V_{diff} \simeq (S_{Ct} - S_{Chr})(T^+ - T^-) = S_{ther}\Delta T. \tag{2.20}$$

S_{ther} and ΔT are defined as $(S_{Ct} - S_{Chr})$ and $(T^+ - T^-)$ respectively. The temperature of the sample is calculated by substitution of equations 2.18 and 2.20 into $T_{avg} = \frac{T^+ + T^-}{2}$:

$$T_{avg} = T_0 + \frac{1}{S_{thr}}(V_{abs} + \frac{V_{diff}}{2}). \tag{2.21}$$

Thermometer method

In this method, two non-calibrated Cernox 1030 thermometers are used. The thermometers are connected to the longitudinal contacts by silver wires and they are suspended with Kevlar wires. In this system T^- and T^+ are measured directly. The ΔT and T_{av} are obtained by :

$$\Delta T = T^+ - T^-$$

and

$$T_{av} = \frac{T^+ + T^-}{2}.$$

The Cernox thermometer's resistance behaves like an insulator. The resistance increases as the temperature decreases, as shown in Figure 2.7. It is most sensitive at low temperatures, but remains fairly accurate up to 300 K.
The Cernox are recalibrated for each measurement to ensure maximum precision, because the calibration may change slightly from one measurement to another. For this purpose, we measure the resistance of the Cernox in heat-off mode ($\dot{Q} = 0$) as a function of temperature. We then fit the curve with a polynominal law to get the calibration (for the calibration, we need to use one that is already calibrate. In our experiment, this is the main thermometer on the mount.). Heat is then applied to generate a thermal gradient and the resistances of the thermomethers are remeasured in order to determine T^+ and T^- using the fitted curve.

2.2.4 Signal analysis

In thermoelectric experiments, we first set the temperature of the probe (T_0), then there are five necessary steps to get data whether in presence or absence of magnetic field:

1. We wait until T_0 and all of the measured voltages are stable. At this stage, no heat current is applied to the sample (heat-off mode).
2. We measure the "background" voltages that exist in thermal equilibrium.
3. We apply a heat current to the sample and wait for the voltages to stabilize again.
4. We measure the heat-on voltages and subtract the background voltages to get the real signal.
5. We remove the heat current from the sample, change T_0 and repeat the whole process.

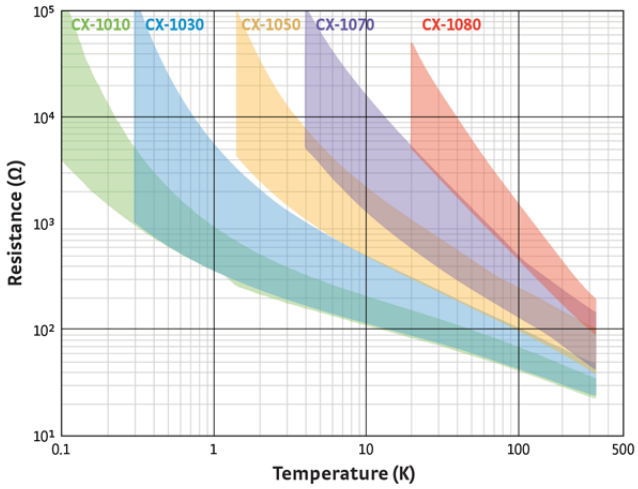

Figure 2.7 Variation of the resistance of different types of Cernox thermometers as a function of temperature, in a log-log scale. https://www.lakeshore.com/products/cryogenic-temperature-sensors/cernox/models/pages/overview.aspx

For field sweep experiments, we stabilize the temperature, measure the background with no heat current, then apply heat and sweep the field from H_{max} to -H_{max}. We then remove the heat, and remeasure the background to ensure that there was no heating effect. Since the Seebeck and Nernst effects can be contaminated by a misalignment of the contacts, it is important to symmetrize and antisymmetrize Seebeck and Nernst coefficients respectively. The Seebeck coefficient is obtained by taking the sum of the longitudinal voltages ΔV_x(+H) and ΔV_x(-H):

$$S = \frac{1}{2}\left(\frac{\Delta V_x(+H)}{\Delta T} + \frac{\Delta V_x(-H)}{\Delta T}\right)$$

and the Nernst coefficient by taking the difference of transverse voltages V_y(+H) and V_y(-H):

$$N = \frac{l}{2w}\left(\frac{\Delta V_y(+H)}{\Delta T} - \frac{\Delta V_y(-H)}{\Delta T}\right)$$

where l is the distance between the longitudinal contacts, w is the width of the sample. This way, the parasite signal from an imperfect alignment of the contacts is removed.

Chapter 3

Transport measurements on LSCO

In this project, I want to explore the link between the pseudogap phase and CDW order in LSCO. Specifically, I want to determine the end point of the CDW phase (p_{CDW}) and see if it is separate from the end point of the pseudogap phase (p^*).

In this chapter, the normal state Hall coefficient and Seebeck coefficient data on various dopings of LSCO single crystals are presented. The LSCO single crystals with doping $x =$ 0.085, 0.11, 0.12 and 0.13 were provided by the University of Bristol, $x = 0.07$ and 0.125 by the University of Tokyo, and $x = 0.144$ and 0.15 by Tohoku University. The transport measurements were performed as described in section 2.2 up to $H = 18$ T at Sherbrooke for all dopings, at the Laboratoire National des Champs Magnétiques Intenses (LNCMI) in Grenoble up to $H = 34$ T for x = 0.07 and 0.144, at the National High Magnetic Field Laboratory (NHMFL) in Tallahassee up to $H = 34$ T for x = 0.125 and 0.15 and up to $H = 45$ T for x = 0.13. The results of this work were published in a Badoux *et al.* [49].

3.1 Hall coefficient

Figure 3.1 shows the prior Hall coefficient data on LSCO as a function of temperature at a doping of $x = 0.12$. Suzuki *et al.* measured $R_H(T)$ of an LSCO single crystal with a magnetic field $H = 9$ T (Figure 3.1 (a)) [36]. They observed a positive $R_H(T)$ at high temperature which then becomes negative at low temperature, displaying the same signature of FSR as in YBCO (see Figure 1.11). Balakirev *et al.* measured $R_H(T)$ of a LSCO thin film with a magnetic field $H = 65$ T [50] but they observed no negative $R_H(T)$. Here is a possible explanation for this difference:

1) The Fermi surface reconstructed by CDW order has a hole-like part in the nodal region and an electron-like part in the antinodal region (Figure 1.17), and it is unclear a prior which part dominates in the Hall signal.
2) The residual resistivity ρ_0 of the single crystal and thin film was around 20 $\mu\Omega cm$ [51] and 80 $\mu\Omega cm$ [50] respectively. The higher value of ρ_0 in the thin film indicates that it is more disordered than in the single crystal. It is possible that this increased disorder would change the relative contribution from hole-like and electron-like regions of the Fermi surface and result in no sign change at low temperature. Note that $R_H(T)$ still drops at low T even in the thin film.

Equation 3.1 shows that when two types of carriers, electrons (e) and holes (h), are involved, the Hall coefficient R_H is given by:

$$R_H = \frac{1}{e}\frac{n_h\mu_h^2 - n_e\mu_e^2}{(n_h\mu_h + n_e\mu_e)^2}, \tag{3.1}$$

where n_e and n_h are electron and hole densities respectively and μ_e and μ_h are electron and hole mobilities respectively. So the type of carrier on the Fermi surface can be distinguished by the sign of the Hall coefficient. This means that, if the Fermi surface is dominated by electron carriers ($\mu_e > \mu_h$), R_H is negative while in the reverse situation when the hole carriers dominate transport on the Fermi surface ($\mu_h > \mu_e$) the sign of R_H will be positive. In thin films, it could be have higher mobility that the hole-like parts in the nodal region dominate the Hall coefficient.

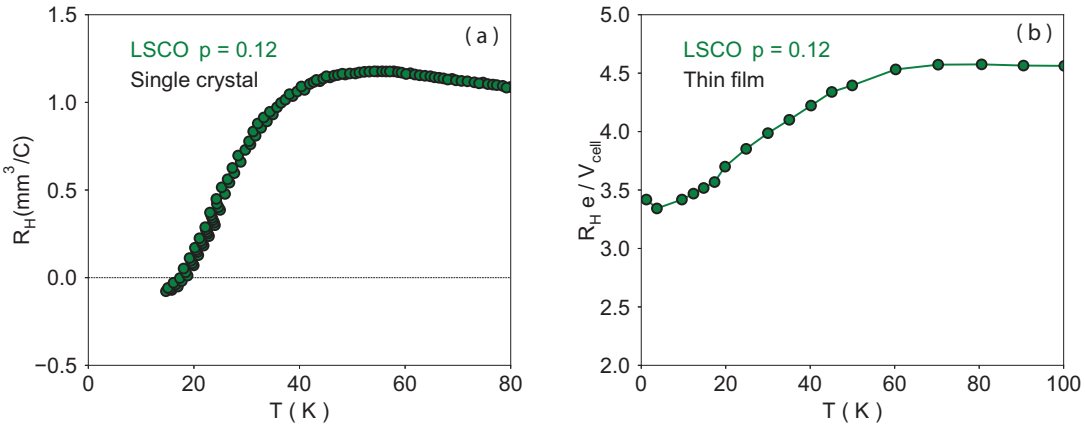

Figure 3.1 (a) Hall coefficient $R_H(T)$ vs temperature T in a single crystal of LSCO at doping $p = 0.12$ and $H = 9$ T becomes negative at low temperature which is indicative of the FSR [36]. (b) $R_H(T)$ in a thin film of LSCO at doping $p = 0.12$, decreases when reducing the temperature but remains positive at $T \to 0$. [50].

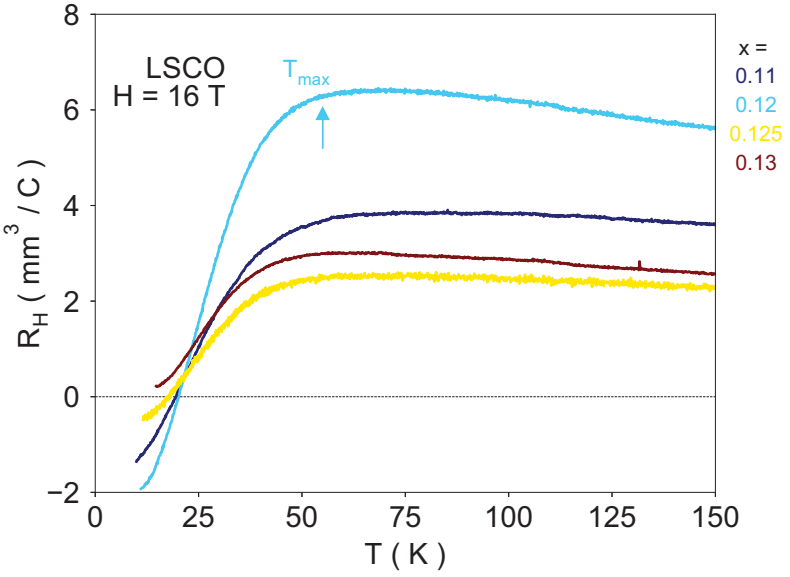

Figure 3.2 Hall coefficient R_H vs Temperature T in LSCO for $x = 0.11$, $x = 0.12$, $x = 0.125$ and $x = 0.13$ at $H = 16$T. At low temperature the R_H of all doping deviates and decreases. R_H in $x = 0.11$, $x = 0.12$ and $x = 0.125$ reaches negative values. For $x = 0.13$ no sign change is observed at low temperature.

In this study, I measured the Hall coefficient of four LSCO single crystal samples. Figure 3.2 shows the temperature dependence of the Hall coefficient for LSCO at dopings $x = 0.11$, $x = 0.12$, $x = 0.125$ and $x = 0.13$ with magnetic field $H = 16$ T.
At dopings $x = 0.11$, $x = 0.12$ and $x = 0.125$ $R_H(T)$ gradually increases when decreasing the temperature down to a temperature T_{max} where it drops and becomes negative at low temperature. This change of sign is observed at $T \simeq 19$ K, 20 K and 18 K for the samples $x = 0.11$, $x = 0.12$, $x = 0.125$ respectively. In section 1.2.3, we have already seen that the negative Hall coefficient at low temperature indicates that the Fermi surface is reconstructed. So it can be concluded that the Fermi surface undergoes a reconstruction in LSCO.

The behavior of the Hall coefficient in my data is in agreement with prior data on an LSCO single crystal at a doping $x = 0.12$ [36]. For $x = 0.13$, $R_H(T)$ shows the same behavior, except that it does not change sign down to $T = 14$ K. Below this temperature, the sample becomes superconducting at this magnetic field.

3.2 Seebeck coefficient

In this section, the Seebeck coefficient is studied. S/T as a function of magnetic field and temperature was measured for dopings $x = 0.07$, 0.085, 0.11, 0.12, 0.125, 0.13, 0.144 and 0.15. At dopings $x = 0.07$ and $x = 0.085$, S/T as a function of magnetic field for different isotherms is shown in Figure 3.3 (a) and (c) respectively. S/T is measured up to $H = 34$ T for $x = 0.07$ and $H = 17.5$ T for $x = 0.085$. For both samples, S/T at the highest measured field keeps increasing with decreasing temperature down to the lowest temperature. S/T versus

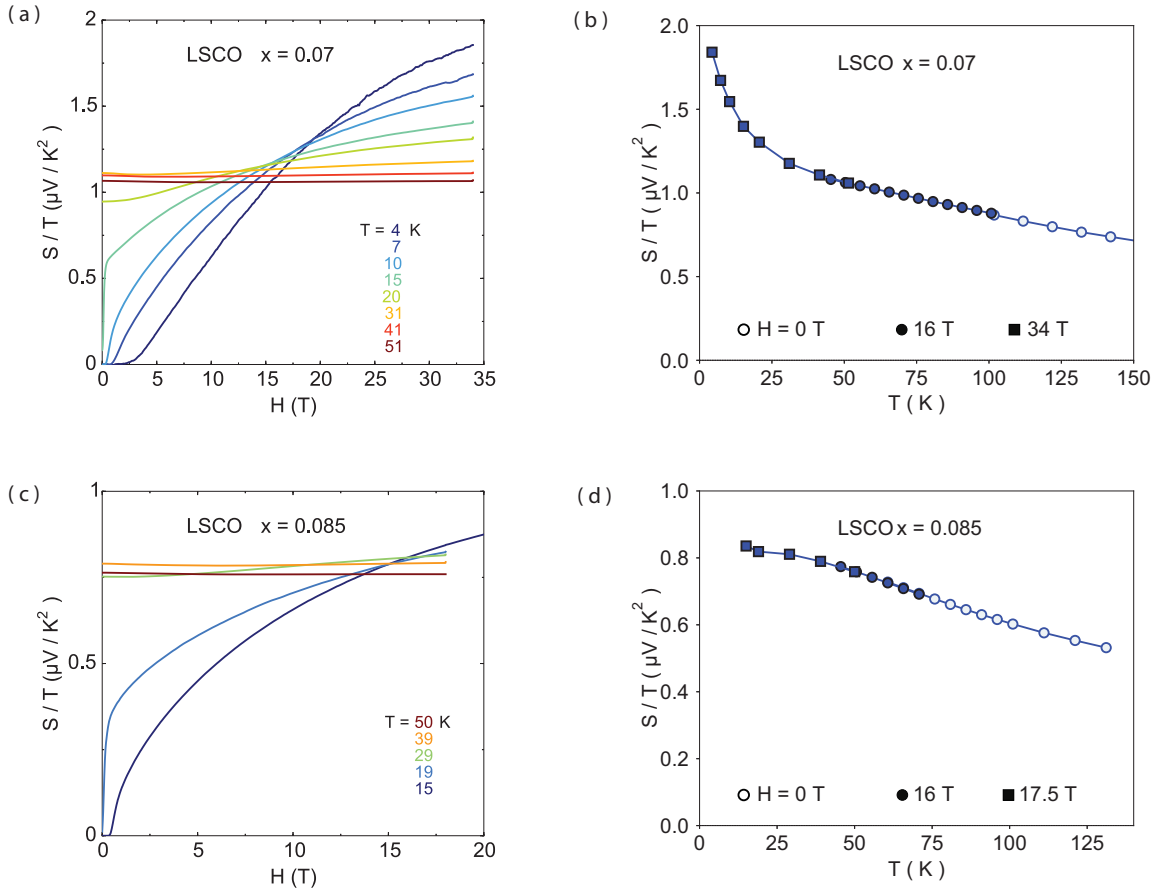

Figure 3.3 The Seebeck coefficient in LSCO at a doping $x = 0.07$ is plotted as (a) S/T vs magnetic field up to 34 T at different temperatures (b) S/T vs temperature at $H = 0$ T (empty circles), $H = 16$ T (full circles) and $H = 34$ T (full squares). The Seebeck coefficient in LSCO at a doping $x = 0.085$ is plotted as (c) S/T vs magnetic field up to 20 T at different temperatures (d) S/T vs temperature at $H = 0$ T (empty circles), $H = 16$ T (full circles) and $H = 17.5$ T (full squares).

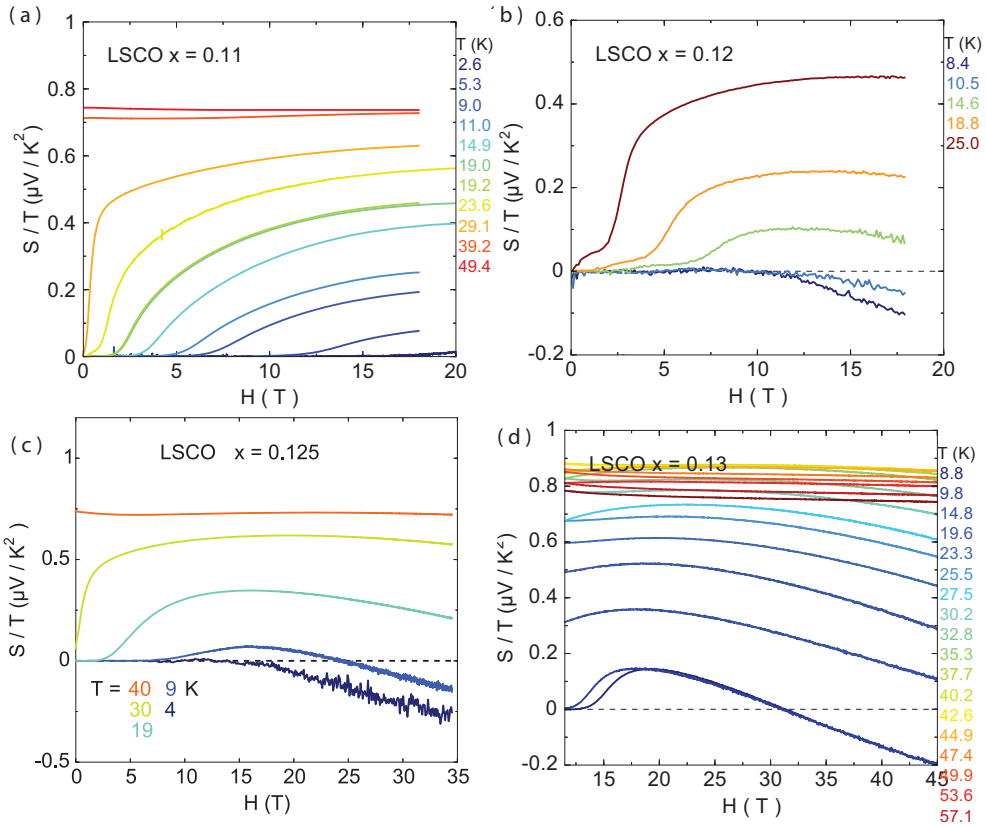

Figure 3.4 The Seebeck coefficient in LSCO, plotted as S/T vs magnetic field at different isotherms for LSCO at doping (a) $x = 0.11$ up to $H = 20$ T (b) $x = 0.12$ up to $H = 17.5$ T (c) $x = 0.125$ up to $H = 34$ T (d) $x = 0.13$ up to $H = 45$ T.

temperature in different magnetic fields is plotted in Figure 3.3(b) and (d) for $x = 0.07$ and $x = 0.085$ respectively. We observe that the normal-state S/T increases monotonically with decreasing T for both samples. This shows that there is no evidence FSR at dopings $x = 0.07$ at least down to 4 K and 0.085 at least down to 15 K.

Figure 3.4 shows S/T versus magnetic field for $x = 0.11$ (up to 20 T), 0.12 (up to 20 T), 0.125 (up to 34 T) and 0.13 (up to 44 T) for different isotherms. For $x = 0.11$, at $H = 17.5$ T, the normal-state S/T increases when temperature increases at least up to ~ 50 K. At dopings $x = 0.12$, 0.125 and 0.13, the behavior of S/T is similar to $x = 0.11$ at highest magnetic field and high temperature. It is roughly flat at low temperature, S/T goes up as a function of field for $x = 0.11$ and it goes down for the others dopings. Figure 3.4 (b), (c) and (d) shows that S/T is negative at very low temperature and its amplitude is increasing with magnetic field. This indicates that this negative value observed is a property of the normal state.

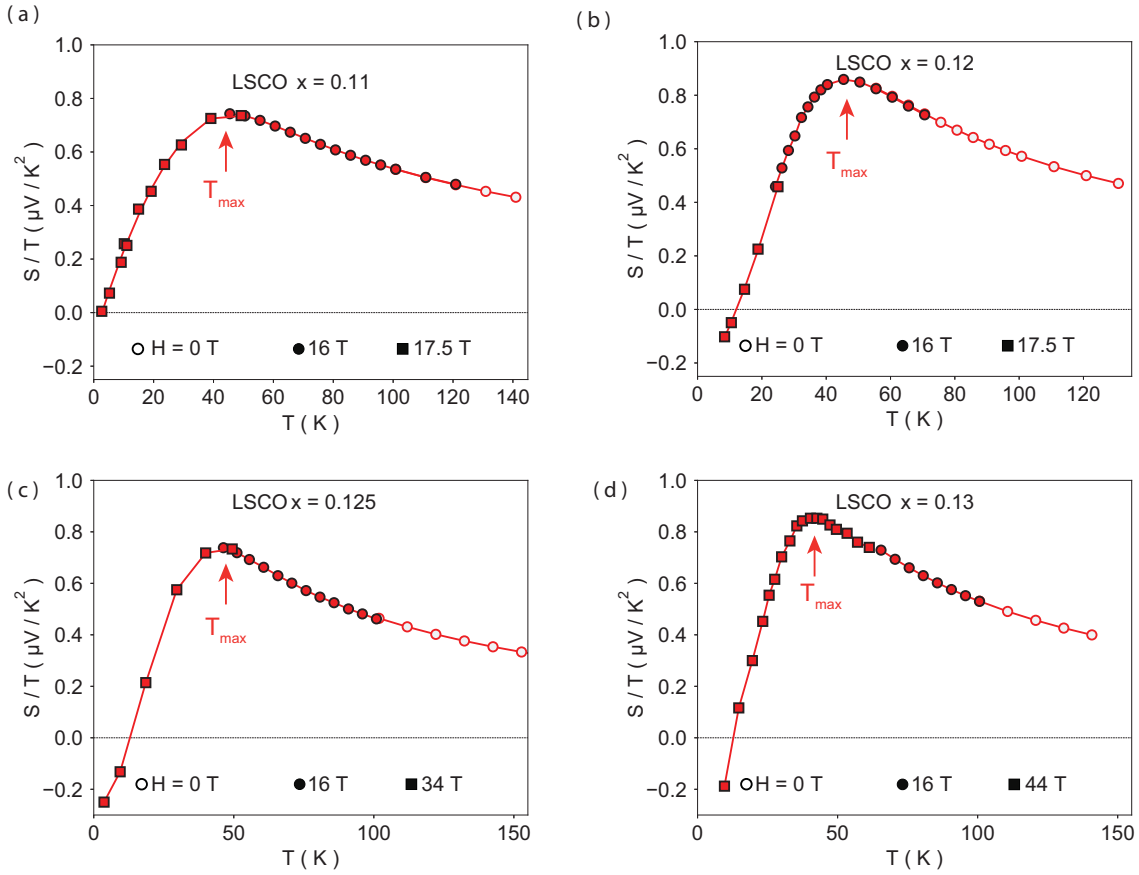

Figure 3.5 The Seebeck coefficient in LSCO, plotted as S/T vs temperature T for LSCO at dopings (a) $x = 0.11$ with magnetic fields $H = 0$ T (empty circles), $H = 16$ T (full circles) and $H = 17.5$ T(full squares), (b) $x = 0.12$ with magnetic fields $H = 0$ T (empty circles), $H = 16$ T (full circles) and $H = 17.5$ T(full squares) (c) $x = 0.125$ with magnetic fields $H = 0$ T (empty circles), $H = 16$ T (full circles) and $H = 34$ T (full squares), (d) $x = 0.13$ with magnetic fields $H = 0$ T (empty circles), $H = 16$ T (full circles) and $H = 44$ T (full squares). For these dopings S/T shows a downturn at T_{max}.

For $x = 0.11$, 0.12, 0.125 and 0.13 dopings, the temperature dependence of S/T in $H = 0$, 16, 34 and 44 T is plotted in Figure 3.5. All these samples show a downturn at T_{max} which is the signature of FSR. The location of these peaks in S/T versus T is seen to decrease from $T_{max} = 41$ K at $x = 0.11$, to $T_{max} = 45$ K at $x = 0.12$, to $T_{max} = 42.5$ K at $x = 0.125$, to $T_{max} = 40$ K at $T_{max} = 0.13$. Moreover, for $x = 0.12$, 0.125 and 0.13, S/T is negative below 10.5 K, 9 K and 10 K respectively.

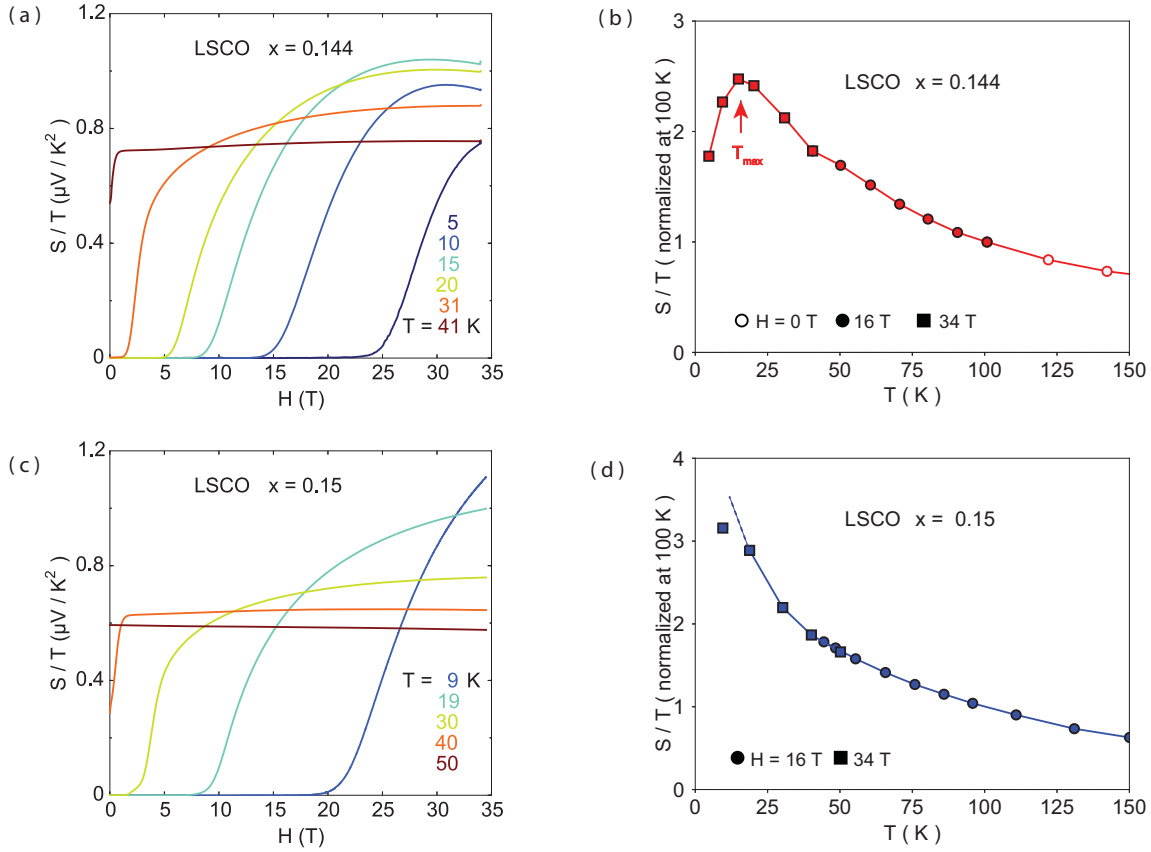

Figure 3.6 The Seebeck coefficient in LSCO at a doping $x = 0.144$ is plotted as (a) S/T vs magnetic field up to 34 T for different isotherms (b) S/T vs temperature at $H = 0$ T (empty circles), $H = 16$ T (full circles) and $H = 34$ T (full squares). S/T shows a downturn at T_{max}. The Seebeck coefficient in LSCO at a doping $x = 0.15$ is plotted as (c) S/T vs magnetic field up to 34 T for different isotherms (d) S/T vs temperature at $H = 0$ T (empty circles), $H = 16$ T (full circles) and $H = 34$ T (full squares).

Figure 3.6 presents S/T as a function of magnetic field and temperature for $x = 0.144$ and $x = 0.15$. At $x = 0.144$, S/T increases at high temperature but then it decreases at low temperatures, below $T_{max} = 15$ K. This decrease is the signature of FSR.

For $x = 0.15$, similarly to $x = 0.07$ and 0.085, S/T at the highest measured magnetic field keeps increasing with decreasing temperature down to the lowest temperature. The downturn in S/T trend continues at $x = 0.144$ where S/T is maximized at $T_{max} \simeq 15$ K while $x = 0.15$ does not show any peak in S/T versus temperature down to 9 K.
This shows that the end point of the Fermi surface reconstruction in LSCO is at a critical

Table 3.1 LSCO - T_{max} vs doping x

x	0.07	0.08	0.11	0.12	0.125	0.13	0.14	0.15
T_{max}	0	0	41	45	42.5	40	15	0

doping $p_{FSR} = 0.15 \pm 0.005$. Table 3.1 shows the value of T_{max} for the eight samples that I measured in this project. T_{max} as a function of doping, which delineates the region where Fermi surface reconstruction occurs, is shown in the phase diagram of LSCO in Figure 3.10. We see that the FSR region peaks at $p \simeq 0.12$ and is confined between $p \simeq 0.085$ and $p = p_{FSR} = 0.15 \pm 0.005$.

3.3 Discussion

As we discussed in Section 1.2, the negative Hall and Seebeck coefficients in the normal state of LSCO are the signature of Fermi surface reconstruction. In addition to LSCO, these signatures of the FSR are also observed in Eu-LSCO [2], Hg1201 [33] and YBCO [52], in the vicinity of $p = 0.12$ (see Figures 1.11 and 1.13).

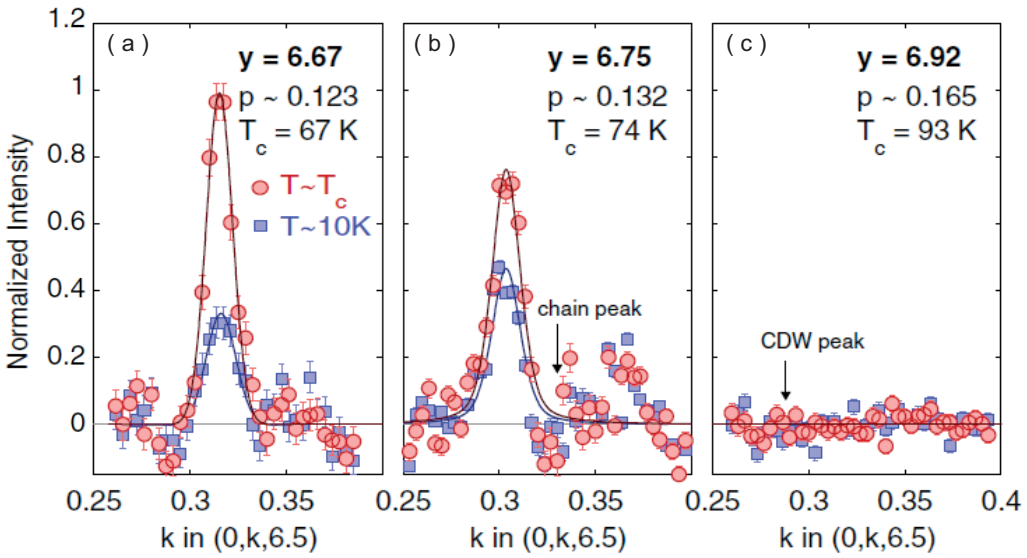

Figure 3.7 CDW peak intensity for YBCO at doping (a) $p \sim 0.123$, (b) 0.132 and (c) 0.165 at zero magnetic field measured at two different temperatures $T \sim T_c$ (red circles) and $T \sim 10$ K (blue squares). Lines through the peaks are least-squares fits using a Gaussian line shape [3].

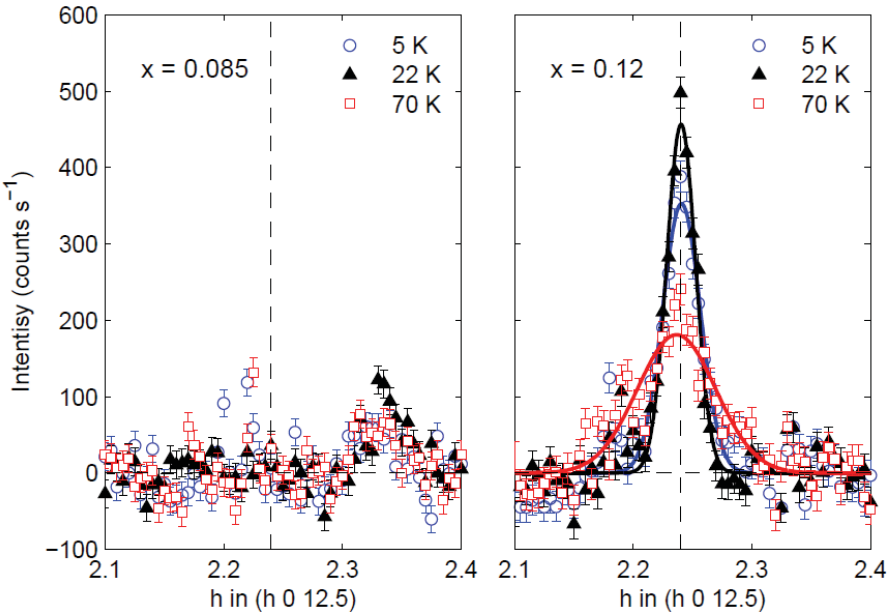

Figure 3.8 CDW peak intensity for LSCO at dopings $x = 0.085$ (left panel) and $x = 0.12$ (right panel) [4] at zero magnetic field measured at three different temperatures $T = 5$ K (blue circles), $T = 22$ K (black triangles) and $T = 70$ K (red squares). Lines through the peaks are fits using a Gaussian line shape (T. Croft and S. M. Hyden, private communication).

Figure 3.7 shows the doping dependence in zero magnetic field of the CDW peak intensity of YBCO at $T = T_c$ and $T \sim 10$ K in XRD measurement [3]. At dopings $p \sim 0.123$ and $p \sim 0.132$ a CDW peak is observed but it disappears at $p \sim 0.165$. In Figure 3.8, the doping dependence in zero magnetic field of the CDW peak intensity of LSCO is shown at $T = 5$ K, 22 K and 70 K. These data are obtained by XRD measurement on LSCO at $x = 0.085$ and 0.12. We see no CDW peaks at a doping $x = 0.085$. In contrast there is an intense CDW peak at $x = 0.12$ [4] where we have observed negative Hall and Seebeck coefficients (Figure 3.8).

Figure 3.9 shows the RIXS [1] for LSCO $x = 0.12$ (12%) and $x = 0.145$ (14.5%) around around (0.25,0) *rlu* [53]. These preliminary XRD data from Zurich university at $x = 0.145$ does not show any CDW peak. X-ray diffraction on LSCO at $x = 0.15$ also does not show a CDW peak (private communication, S. M. Hyden). The link between CDW and FSR is clear: the FSR occurs in a region of the $T - p$ phase diagram where CDW modulations have been detected by XRD, as shown in Figure 3.10.

[1] Resonant inelastic X-ray scattering

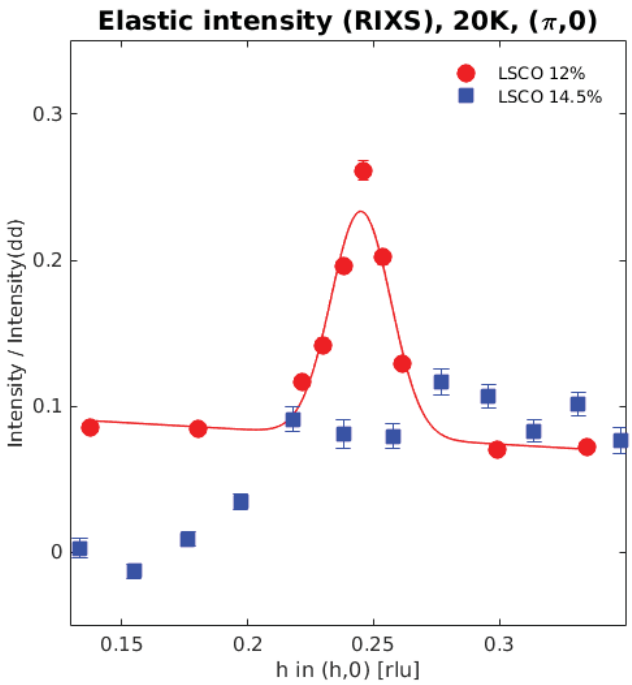

Figure 3.9 The comparison of CDW peak intensity for LSCO at dopings $x = 0.12$ (12% and red circles) and $x = 0.145$ (14.5% and blue squares with RIXS measurement) at zero magnetic field measured in $T = 20$ K [53].

If we compare YBCO and LSCO phase diagrams (Figure 3.10), we see that, in both cases, T_{CDW} and T_{max} are peaked at $p = 0.12$ and the FSR is confined to similar ranges of doping: $0.08 \leq p \leq 0.16$ and $0.085 \leq p \leq 0.15$ for YBCO [27] and LSCO respectively. Figure 3.11 shows the X-ray, Seebeck coefficient and Hall coefficient measurements for YBCO and LSCO at $p = 0.12$. In Figure 3.11(a), the XRD detects the CDW modulation in YBCO at $T_{CDW} \simeq 150$ K and for LSCO at $T_{CDW} \simeq 75$ K which reveals that T_{CDW} in YBCO is twice as high as T_{CDW} in LSCO. Figure 3.11 (b) and (c) also show that the FSR is detected up to a temperature two times as high in YBCO with $T_{max} \simeq 100$ K in YBCO and $T_{max} \simeq 50$ K in LSCO. Interestingly, the superconducting transition temperature T_c in YBCO is roughly twice as high in YBCO as in LSCO. This raises the interesting possibility that the same underlying mechanism, perhaps magnetic, fuels both superconductivity and CDW order [57].

In the above, we discussed the existence of a relationship between FSR and CDW modulation. Consequently, in LSCO, the end of CDW order is same as where the FSR ends at $p_{FSR} = 0.15$. This is what was also observed by X-ray diffractions that there is no CDW modulation at $x = 0.15$ so we can also consider the $p_{CDW} = 0.15$ as the end of charge order in LSCO. Additionally, the in-plane resistivity of LSCO at high magnetic field indicates that

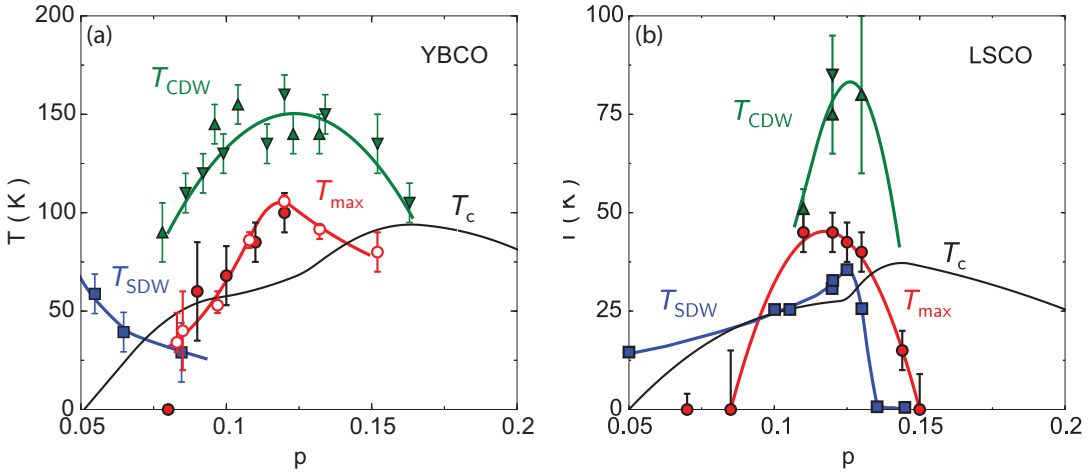

Figure 3.10 $T-p$ phase diagram of (a) YBCO and (b) LSCO. The superconducting transition temperature T_c is drawn as a black line. CDW modulations are detected by x-ray diffraction below T_{CDW} (green triangles) in YBCO (up triangles [3], down triangles [41]) and LSCO (up triangles [4], down triangle [54]). SDW modulations are detected by neutron diffraction below T_{SDW} (blue squares) in YBCO [55] and LSCO [14, 15, 17, 18, 16]. When plotted as S/T vs T, the normal-state Seebeck coefficient peaks at a temperature T_{max} (full red circles) before it drops at low temperatures because of Fermi surface reconstruction (YBCO [2] and LSCO is presented in this study as Figures 3.3, 3.5 and 3.6). A similar T_{max} can also be defined for YBCO in the Hall coefficient (open red circles), below which $R_H(T)$ drops at low temperatures [56].

the pseudogap ends at $p^* = 0.185 \pm 0.005$ [43]. Since $p^* > p_{CDW}$ it is clear that these two phases are distinct from each other. This clear separation reveals that the pseudogap phase is not caused by the CDW ordering. Instead, it suggests that CDW order is a secondary instability of the pseudogap phase.

This separation is also seen in YBCO by Hall effect measurements where $p_{CDW} = 0.16 \pm 0.005$ and $p^* \simeq 0.19$ [27]. This strongly suggests that a separation of p_{CDW} and p^* is a generic property of cuprates.

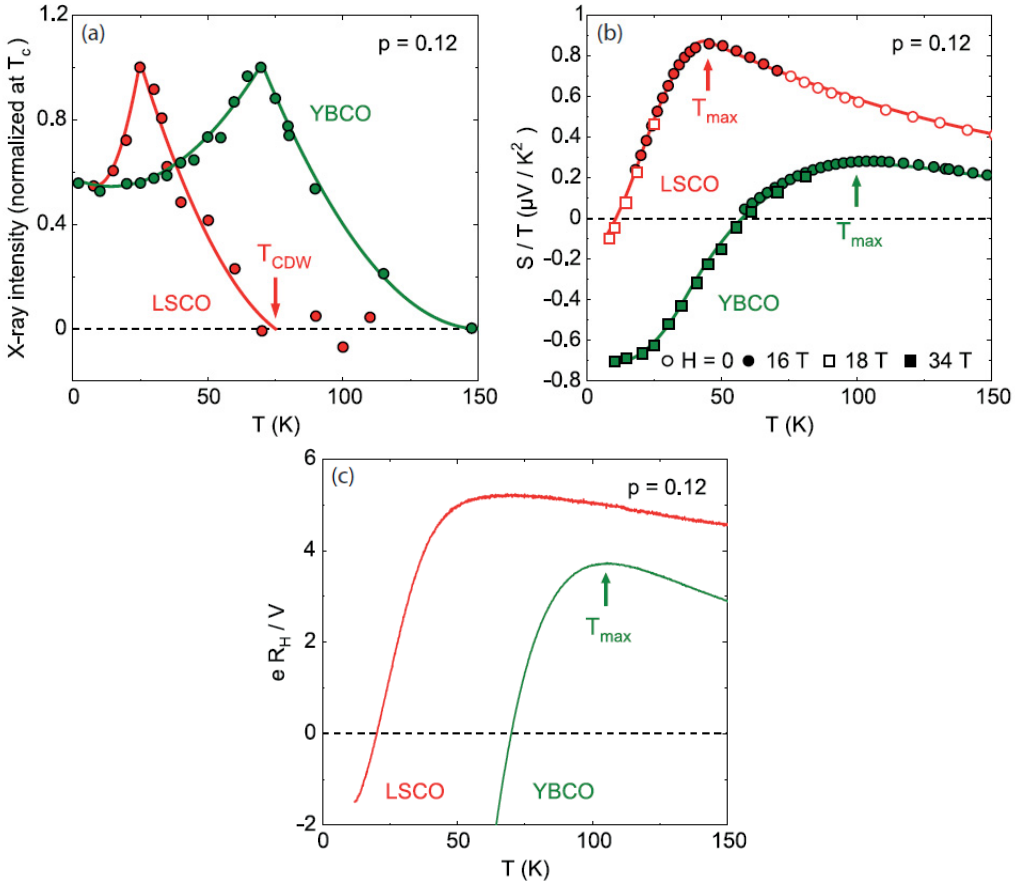

Figure 3.11 Comparison of LSCO (red) and YBCO (green) at $p = 0.12$. (a) Temperature dependence of the X-ray intensity associated with the CDW modulations, normalized at T_c, detected in LSCO [4] and YBCO [20]. Lines are a guide to the eye. The cusp is at T_c. (b) Normal-state Seebeck coefficient of LSCO (this work) and YBCO [2], in the indicated magnetic fields plotted as S/T vs temperature. T_{max} is the temperature below which S/T drops to reach negative values at low temperatures (arrow), the signature of FSR. This T_{max} is plotted as full circles in Figure 3.10. Lines are a guide to the eye. (c) Hall coefficient of LSCO at $H = 16$ T and YBCO at $H = 15$ T [1], plotted as eR_H/V, where e is the electron charge and V the volume per planar Cu atom. T_{max} is the temperature below which $R_H(T)$ drops to reach negative values at low temperatures (arrow), another signature of FSR. T_{max} is plotted as open circles in Figure 3.10 (a) [56].

Conclusion

The main motivation of this project was finding the link between the pseudogap phase and charge density wave order in the cuprate superconductor LSCO.
To this end we pinned down the end point of the CDW (p_{CDW}) region in the phase diagram by using transport measurements such as the Hall effect and the Seebeck coefficient. These measurements required high magnetic field in order to suppress the superconductivity and access to the normal state at very low temperature.

Our results from Seebeck coefficient measurements show that the Fermi surface is reconstructed at low temperature in the range $0.085 < p < 0.15$. The remarkable similarity of the doping dependence of the Fermi surface reconstruction has been already detected in three other materials as YBCO, Eu-LSCO and Hg1201 cuprates. As we have seen in the cuprates mentioned above, this FSR connects to the CDW modulation detected by XRD since both are observed in the same doping range.

In agreement with XRD, our Seebeck data indicate that the CDW modulations disappear at $p = p_{CDW} = 0.15$, so the field-induced non-superconducting ground state of LSCO above $p = 0.15$ has no CDW order. In this compound the pseudogap phase extends up to $p \simeq 0.18$. Previous studies on YBCO superconductors also showed that its CDW modulation ends at $p = 0.16$, while the pseudogap critical point is at $p^* \simeq 0.19$. Consequently, we infer that the pseudogap is not tied to CDW ordering. Instead, the CDW modulations appear to be a secondary instability of the pseudogap phase.

Appendix A

Calculation of Seebeck and Nernst coefficients

Seebeck coefficient

$$\boldsymbol{J}^e = -\sigma \boldsymbol{\nabla} V - \alpha \boldsymbol{\nabla} T \tag{A.1}$$

Where σ is electrical conductivity, α is the Peltier coefficient, $\nabla V = -E$ and T is the temperature. For thermoelectric transport, the electric current density J^e along x, y direction is:

$$\begin{bmatrix} J_x \\ J_y \end{bmatrix} = \begin{bmatrix} \sigma_{xx} & \sigma_{xy} \\ \sigma_{yx} & \sigma_{yy} \end{bmatrix} \begin{bmatrix} E_x \\ E_y \end{bmatrix} - \begin{bmatrix} \alpha_{xx} & \alpha_{xy} \\ \alpha_{yx} & \alpha_{yy} \end{bmatrix} \begin{bmatrix} \partial_x T \\ \partial_y T \end{bmatrix}. \tag{A.2}$$

To measure the Seebeck coefficient, no electrical current is applied to the sample, $J_e = 0$:

$$\begin{bmatrix} 0 \\ 0 \end{bmatrix} = \begin{bmatrix} \sigma_{xx} E_x + \sigma_{xy} E_y \\ \sigma_{yx} E_x + \sigma_{yy} E_y \end{bmatrix} - \begin{bmatrix} \alpha_{xx} \partial_x T + \alpha_{xy} \partial_y T \\ \alpha_{yx} \partial_x T + \alpha_{yy} \partial_y T \end{bmatrix}. \tag{A.3}$$

We neglect the thermal gradient along y as it is orders of magnitude smaller than along x:

$$\sigma_{xx} E_x + \sigma_{xy} E_y - \alpha_{xx} \partial_x T = 0 \tag{A.4}$$

and,

$$\sigma_{yx}E_x + \sigma_{yy}E_y - \alpha_{yx}\partial_x T = 0. \tag{A.5}$$

We extract E_y from A.5:

$$E_y = \frac{1}{\sigma_{yy}}(\alpha_{yx}\partial_x T - \sigma_{yx}E_x). \tag{A.6}$$

By substituting A.6 into A.4:

$$E_x(\sigma_{xx} - \sigma_{xy}\frac{\sigma_{yx}}{\sigma_{yy}}) - \partial_x T(-\alpha_{yx}\frac{\sigma_{xy}}{\sigma_{yy}} + \alpha_{xx}) = 0. \tag{A.7}$$

The Seebeck coefficient is simply defined as:

$$S \equiv \frac{E_x}{\partial_x T}. \tag{A.8}$$

We consider that $\sigma_{xx} = \sigma_{yy}$ and $\alpha_{xx} = \alpha_{yy}$ due to the symmetries of an isotropic system (for a tetragonal system) and $\sigma_{yx} = -\sigma_{xy}$ because of time reversal symmetry, the equation A.7 is written:

$$S = \frac{\alpha_{xx}\sigma_{xx} + \alpha_{xy}\sigma_{xy}}{\sigma_{xx}^2 + \sigma_{xy}^2}. \tag{A.9}$$

The Seebeck coefficient is related to the conductivity σ and thermoelectricity coefficients α. The solution of Boltzmann equation at low temperature connects σ and α. This equation is true when there is a temperature gradient due to heat flowing from a hot region to a cold one.

$$\alpha_{ij} = -\frac{\pi^2}{3}\frac{k_B^2 T}{e}\frac{\partial\sigma_{ij}(\epsilon)}{\partial\epsilon}\,|_{\epsilon=\epsilon_F} \tag{A.10}$$

In absence of a magnetic field, $\sigma_{xy} = 0$ and $\alpha_{xy} = 0$, then A.9 becomes:

$$S \approx \frac{\alpha_{xx}}{\sigma_{xx}}. \tag{A.11}$$

Nernst coefficient

The Nernst effect is a thermoelectric phenomenon where when a magnetic field (H) is applied along the z direction and perpendicularly to the temperature gradient ($\nabla_x T$), the

carriers deviate transversely and generate a potential difference (ΔV_y). So the Nernst effect is defined as:

$$N = -\frac{\Delta V_y}{\partial_x T}. \tag{A.12}$$

E_x is extracted from A.5:

$$E_x = \frac{1}{\sigma_{yx}}(-\sigma_{yy}E_y + \alpha_{yx}\partial_x T) \tag{A.13}$$

and then A.13 is substituted in A.4:

$$E_y(\sigma_{xy} + \frac{\sigma_{xx}^2}{\sigma_{xy}}) + \partial_x T(\frac{\sigma_{xx}}{\sigma_{xy}}\alpha_{xy} - \alpha_{xx}) = 0. \tag{A.14}$$

The Nernst coefficient is then given by:

$$N \equiv \frac{-E_y}{\partial_x T}. \tag{A.15}$$

With respect to the symmetries of isotropic system ($\sigma_{xx} = \sigma_{yy}$ and $\alpha_{xx} = \alpha_{yy}$) and time reversal symmetry ($\sigma_{xy} = -\sigma_{yx}$), A.15 can be extended:

$$N = \frac{\alpha_{xy}\sigma_{xx} - \alpha_{xx}\sigma_{xy}}{\sigma_{xx}^2 + \sigma_{xy}^2}. \tag{A.16}$$

If we consider the assumption that $\sigma_{xy}^2 \ll \sigma_{xx}^2$ [46], equation A.16 will be written:

$$N \simeq \frac{\alpha_{xy}\sigma_{xx} - \alpha_{xx}\sigma_{xy}}{\sigma_{xx}^2}. \tag{A.17}$$

Combining A.11 and A.17 with the definition of the Hall angle ($tan\theta_H = \frac{\sigma_{xy}}{\sigma_{xx}}$) yields:

$$N \simeq \frac{\alpha_{xy}}{\sigma_{xx}} - S\tan\theta_H. \tag{A.18}$$

The Boltzmann equation at low temperature (A.10) is also used to find the arrays of σ and α and is combined with equation (A.17):

$$N = -\frac{\pi^2}{3}\frac{k_B^2 T}{e}\frac{\partial tan\theta_H}{\partial \epsilon}\ |_{\epsilon=\epsilon_F}\ . \tag{A.19}$$

We assume that the Hall angle depends linearly on energy in the vicinity of the Fermi energy.

So the derivative can be approximately evaluated at ϵ_F by $\frac{\tan\theta_H}{\epsilon_F}$. For a single band system, $tan\theta_H = \mu B$, and the Nernst coefficient ν is described by:

$$\nu = \frac{N}{B} = \pm\frac{\pi^2}{3}\frac{k_B^2 T}{e}\frac{\mu}{\epsilon_F}. \tag{A.20}$$

This shows that the Nernst signal is directly proportional to the magnetic field and mobility and it is also inversely proportional to ϵ_F. In other words, the Nersnt signal is able to show the ratio of scattering time τ over carrier density n by using; mobility $\mu = e\tau/m^*$ and the density of states in 3-D $N(\epsilon) = 3n/2\epsilon_F$ [58].

Appendix B

LSCO - Seebeck and Nernst coefficients

In addition to the dopings of LSCO mentioned in the previous chapters, this study involved investigating a wide range of dopings in LSCO in thermopower experiments.
In this section the data of S/T and N/T will be presented in a range of doping between $x = 0.06$ and $x = 0.30$ at zero and 16 T magnetic field. LSCO $x = 0.16, 0.20$ were also studied in high magnetic fields of $H = 33.5$ T and 24 T.

B.1 Seebeck coefficient

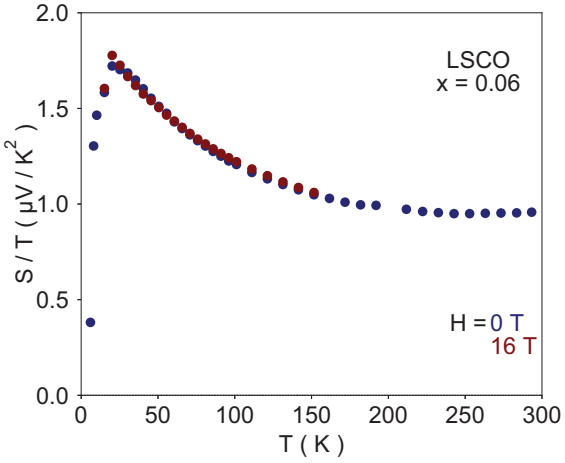

Figure B.1 Seebeck measurement as a function of temperature in LSCO x =0.06 at $H = 0$ and 16 T.

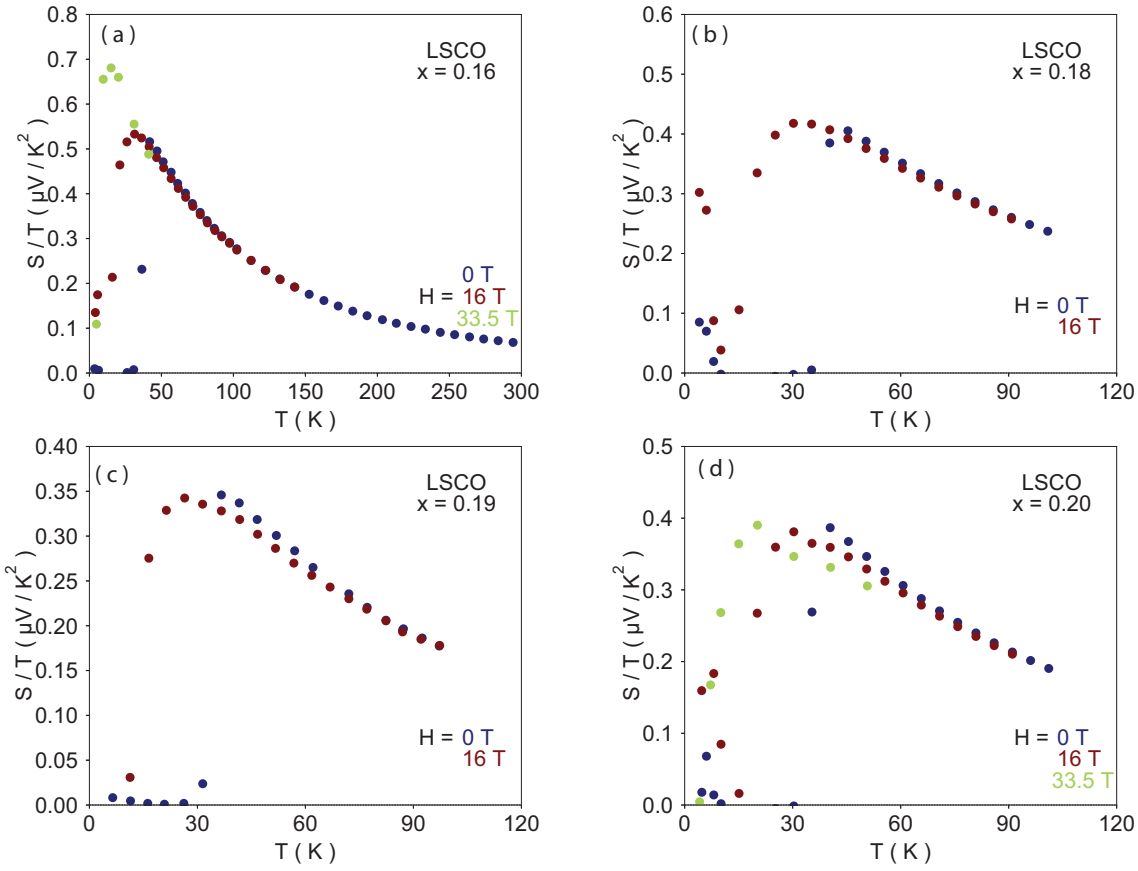

Figure B.2 Seebeck measurement as a function of temperature in LSCO (a)x =16, (d) $x = 0.20$ at $H = 0$, 16T and 33.5T, (b) $x = 0.18$, (c) $x = 0.19$ at $H = 0$ and 16 T.

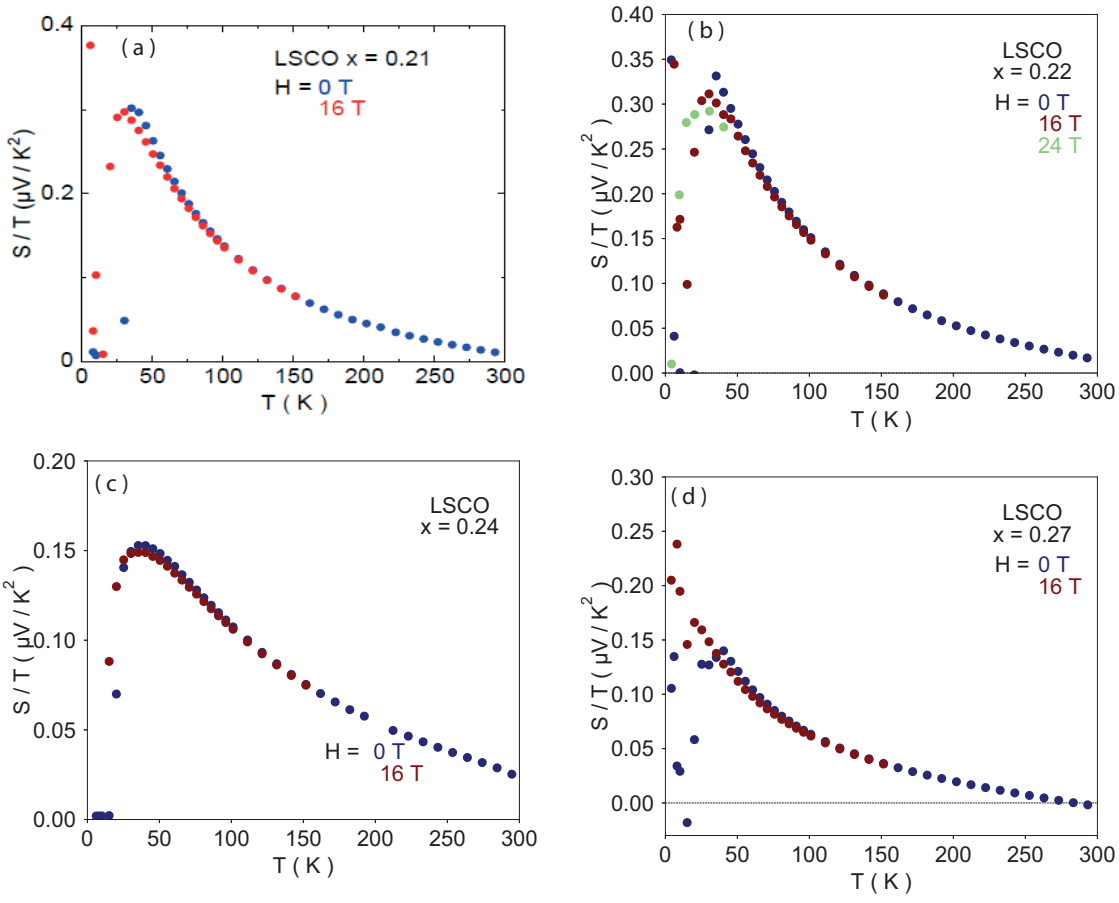

Figure B.3 Seebeck measurement as a function of temperature in LSCO (a)x =21, (c) $x = 0.24$ and (d) $x = 0.27$ at $H = 0$ and 16T (b) $x = 0.22$ at $H = 0$, 16T and 24 T.

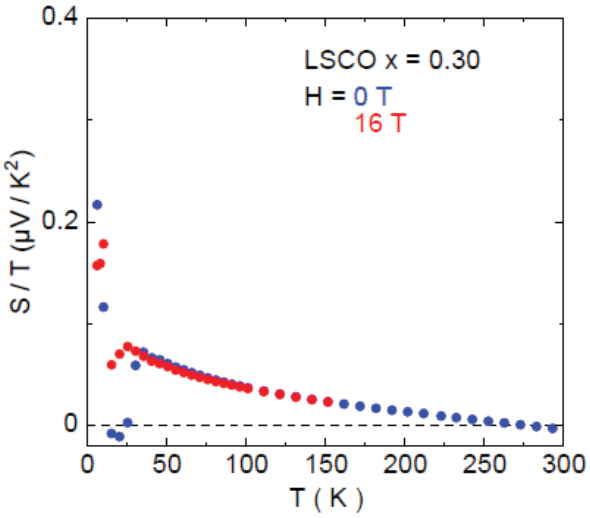

Figure B.4 Seebeck measurement as a function of temperature in LSCO x =0.30 at $H = 0$ and 16 T.

B.2 Nernst coefficient

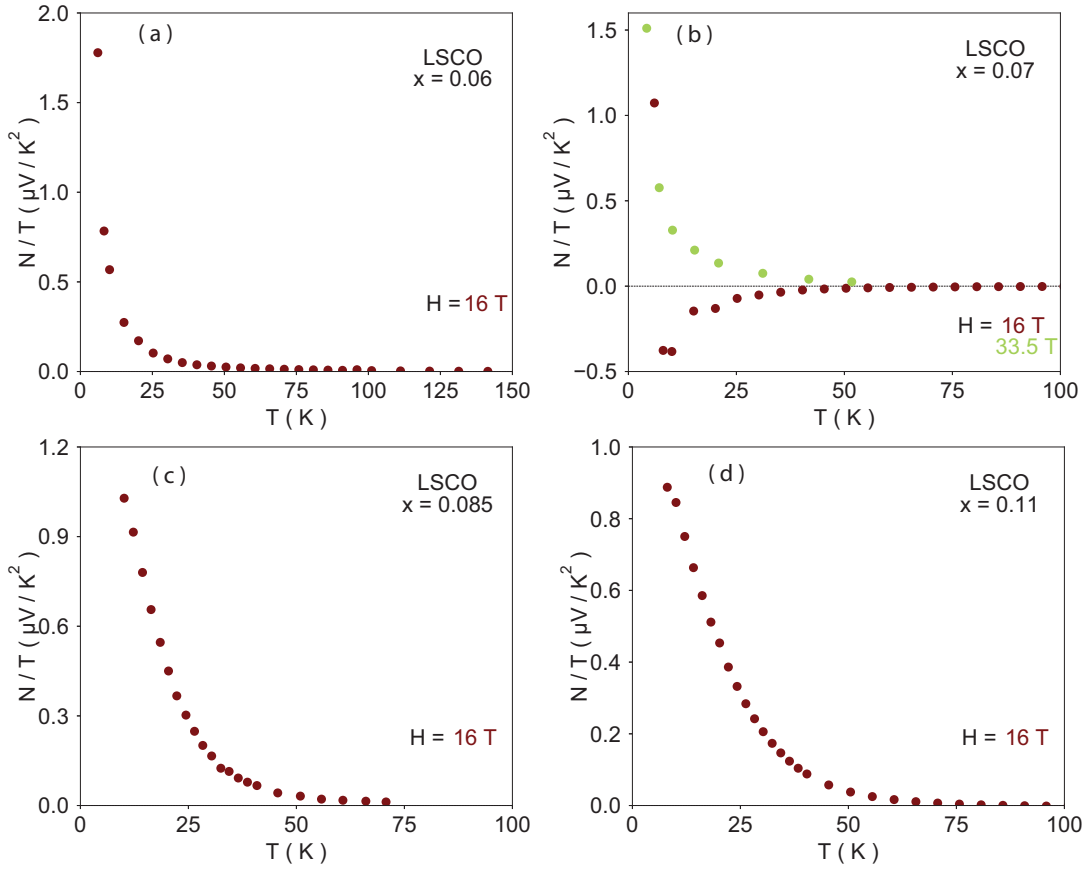

Figure B.5 Nernst measurement as a function of temperature in LSCO (a) x =0.06, (c) $x = 0.11$ and (d) $x = 0.085$ at $H = 16$T (b) $x = 0.07$ at $H = 16$T and 33.5 T.

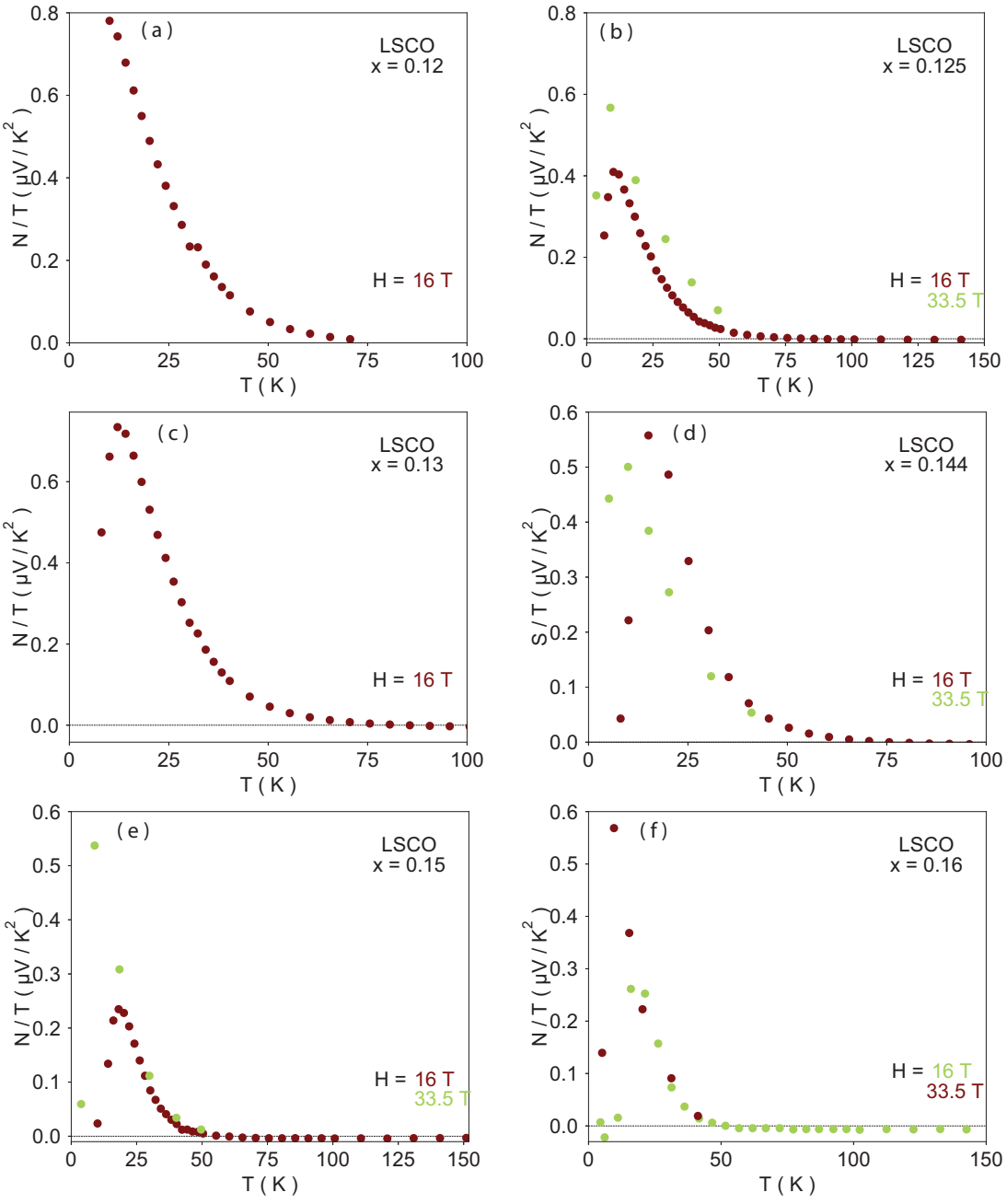

Figure B.6 Nernst measurement as a function of temperature in LSCO (a) x =0.12, (c) $x = 0.13$ at $H = 16$ T, (b) $x = 0.125$, (d) $x = 0.144$, (e) $x = 0.15$ and (f) $x = 0.16$ at $H = 16$T and 33.5 T.

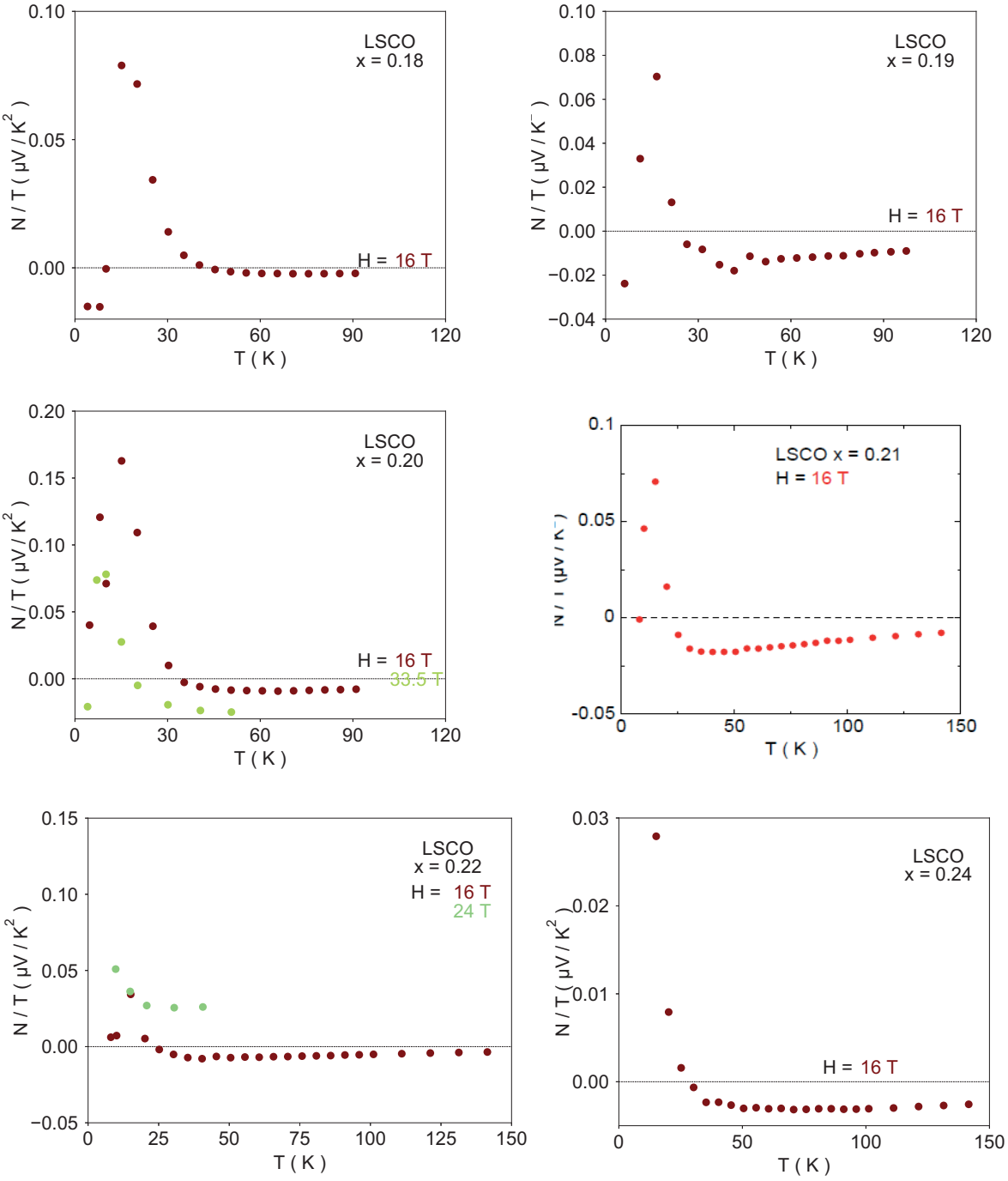

Figure B.7 Nernst measurement as a function of temperature in LSCO (a) x =0.18, (b) x = 0.19, (d) $x = 0.21$, (f) $x = 0.24$ at $H = 16$ T, (c) $x = 0.20$ at $H = 16$ T and 33.5 T, (e) $x = 0.22$ at $H = 16$T and 24 T.

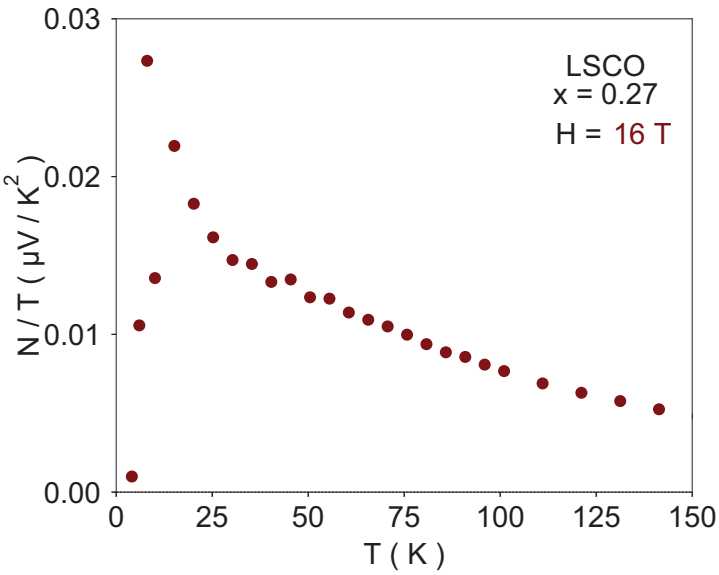

Figure B.8 Nernst measurement as a function of temperature in LSCO x =0.27 at $H = 16$ T.

Appendix C

LSCO - Electrical resistivity and Hall effect

In this project, we have also studied the resistivity and Hall effect in LSCO for various dopings at zero and 16 T magnetic field.

C.1 Electrical resistivity

Considering the definition of superconductivity, the resistivity measurement is mostly used to find the critical temperature T_c in superconductors. In Figure 2.1, it is sketched that the electrical resistivity (ρ_{xx}) is the generation of a longitudinal voltage (ΔV_x) to an electrical current along the same direction I_x in the sample. The resistivity is obtained by Equation C.1:

$$\rho_{xx} = \frac{\Delta V_x}{I_x}\frac{wt}{L} \tag{C.1}$$

where w, t and L are the width, thickness and length of the sample, respectively. The geometrical factors of LSCO for different dopings, T_c [1] and where they came from are shown in Table C.1.

We measured the electrical resistivity of LSCO for a wide range of doping from the underdoped region ($x = 0.07, 0.11, 0.12, 0.125, 0.13$ and 0.144 (Figure C.1)) to optimal doping ($x = 0.15$) and overdoped region ($x =$0.16, 0.20 and 0.24 (Figure C.2)) at $H = 0$ and 16 T.

[1] The critical temperature of a superconductor is determined by the point where resistivity goes to zero at $H = 0$ T.

Table C.1 Characteristics of our LSCO single crystal: Sr content x, length between contacts l, width w, thickness t, geometric factor $\alpha = wt/l$, critical temperature T_c where $R = 0$ and the group in which sample was grown.

x	l (μm)	w (μm)	t (μm)	α (cm)	T_c (K)	Group
0.06	759	720	189	45×10^{-3}	4 ± 0.5	Takagi (Tokyo)
0.07	866	410	55	2.6×10^{-3}	12 ± 0.4	Takagi (Tokyo)
0.11	1198	455	103	3.9×10^{-3}	26 ± 0.8	Hayden (Bristol)
0.12	920	450	90	4.4×10^{-3}	27.5 ± 1	Hayden (Bristol)
0.125	2141	766	331	11.8×10^{-3}	28 ± 1	Takagi (Tokyo)
0.13	1924	467	93	2.2×10^{-3}	31 ± 0.3	Hayden (Bristol)
0.144	1794	824	178	8.2×10^{-3}	37 ± 0.15	Yamada (IMSS)
0.15	2559	658	440	11.3×10^{-3}	38 ± 0.6	Yamada (IMSS)
0.16	620	380	82	5.0×10^{-3}	35.5 ± 0.25	Takagi (Tokyo)
0.18	1556	1807	233	27×10^{-3}	-	Yamada (IMSS)
0.19	1316	330	370	9.3×10^{-3}	-	Takagi (Tokyo)
0.20	1140	233	167	3.4×10^{-3}	31 ± 0.5	Takagi (Tokyo)
0.21	1615	342	447	9.5×10^{-3}	-	Takagi (Tokyo)
0.22	1039	663	723	46.1×10^{-3}	-	Takagi (Tokyo)
0.24	1663	841	292	14.8×10^{-3}	15 ± 0.25	Takagi (Tokyo)
0.27	1372	662	76	3.7×10^{-3}	-	Yamada (IMSS)
0.30	1422	517	89	3.2×10^{-3}	-	Yamada (IMSS)

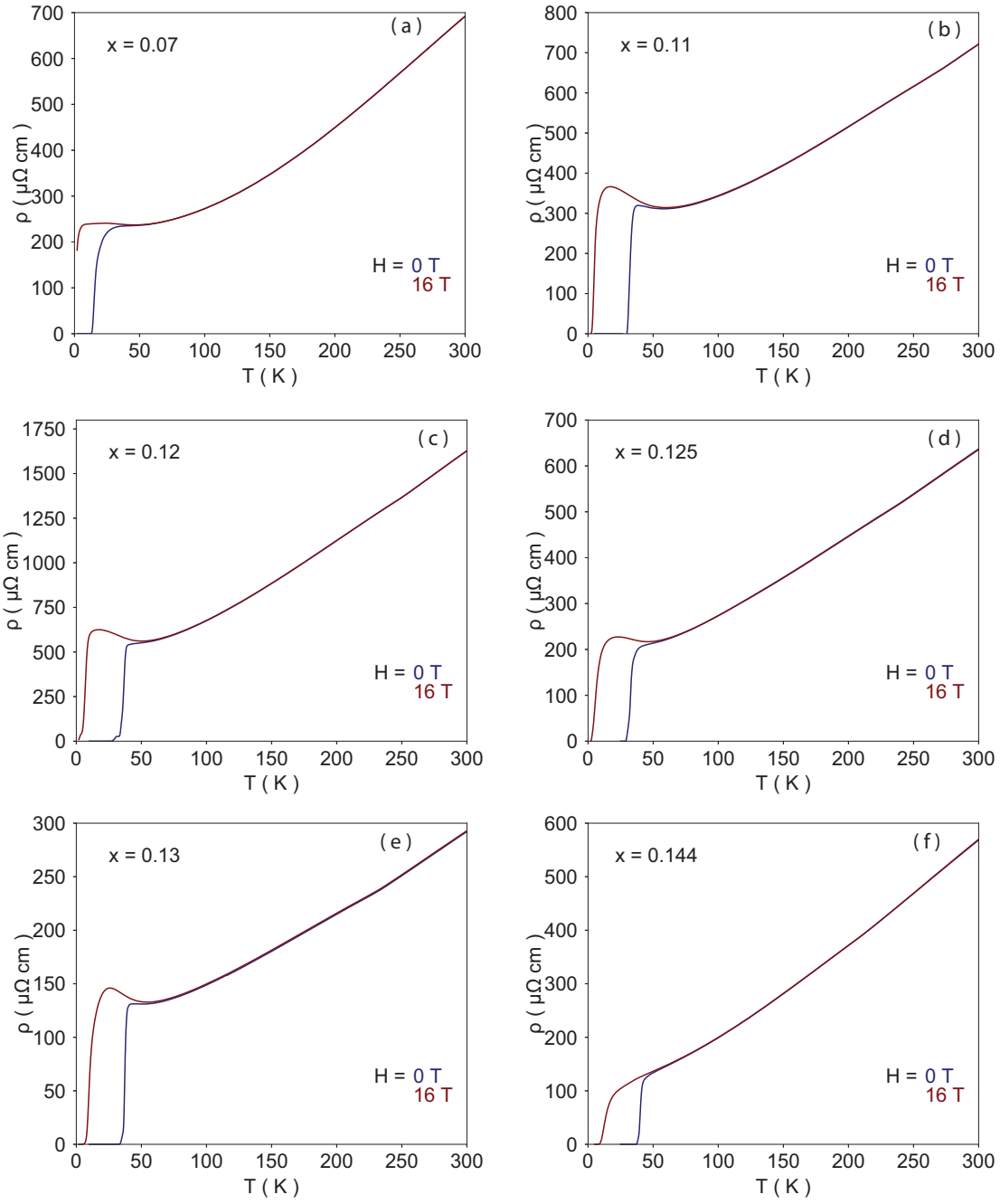

Figure C.1 The LSCO electrical resistivity measurements in the underdoped region $x = 0.07$ (a), $x = 0.11$ (b), $x = 0.12$ (c), $x = 0.125$ (d), $x = 0.13$ (e), and $x = 0.144$ (f) at magnetic field $H = 0$ and 16 T.

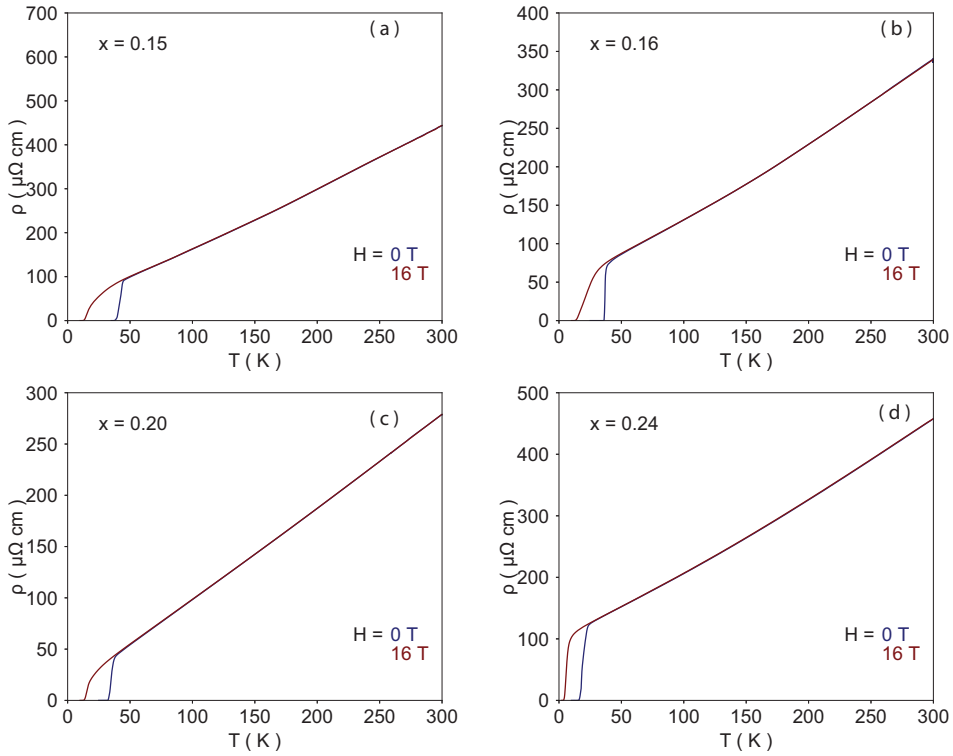

Figure C.2 The LSCO electrical resistivity measurements in the optimally doped $x = 0.15$ (a) and overdoped region $x = 0.16$ (b), $x = 0.20$ (c) and $x = 0.24$ (d) at magnetic field $H = 0$ and 16 T.

C.2 Hall effect

The measurement of the Hall coefficient is a satisfying probe to determine the Fermi surface reconstruction and the type of carriers which contribute to transport on the Fermi surface as explained in Chapter 2. The Hall effect has been already shown in LSCO at $x = 0.11$, 0.12, 0.125 and 0.125 at $H = 16$ T in Section 3.2. We also measured it for $x = 0.144$, 0.15, 0.16, 0.20 and 0.24 at $H = 16$ T (Figure C.3).

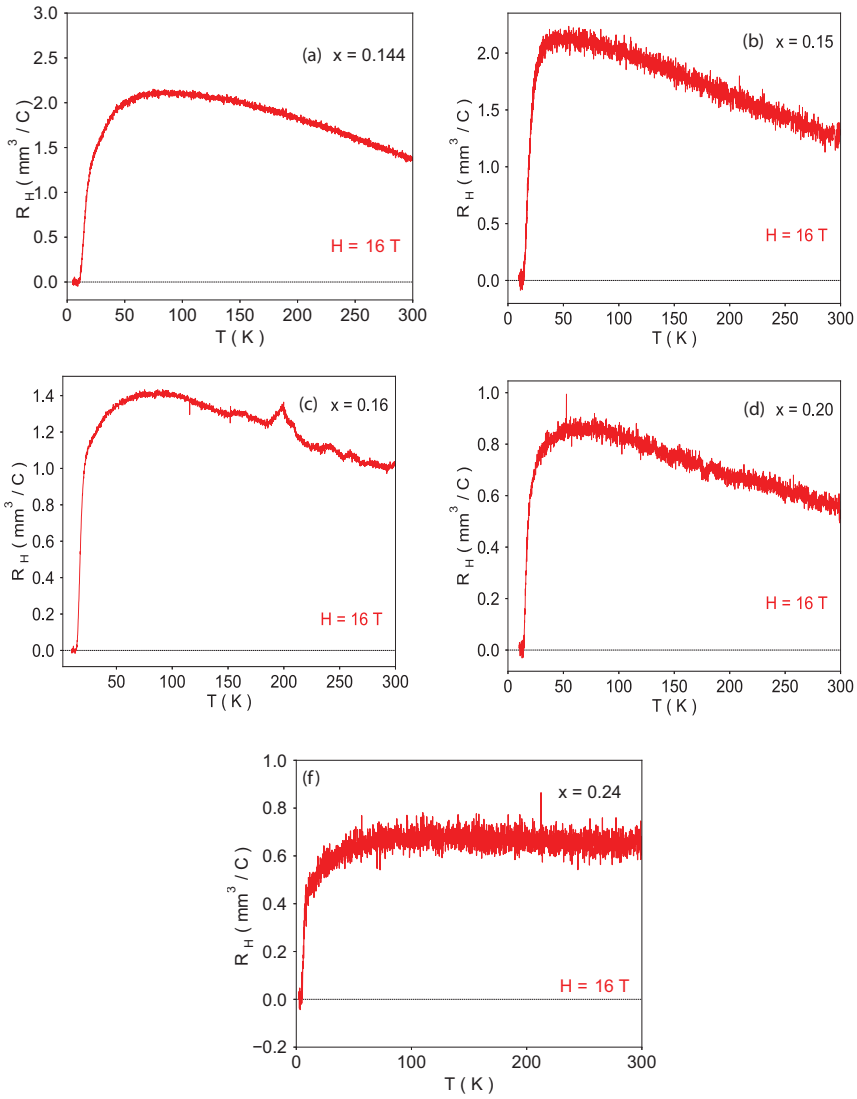

Figure C.3 LSCO Hall coefficient R_H for $x = 0.144$ (a), $x = 0.15$ (b), $x = 0.16$ (c), $x = 0.20$ (d) and $x = 0.24$ (e) at magnetic field $H = 16$ T.

Bibliography

[1] LeBoeuf, D., Doiron-Leyraud, N., Levallois, J., Daou, R., Bonnemaison, J.-B., Hussey, N. E., Balicas, L., Ramshaw, B. J., Liang, R., Bonn, D. A., Hardy, W. N., Adachi, S., Proust, C., and Taillefer, L. *Nature* **450**, 533–536 November (2007).

[2] Laliberté, F., Chang, J., Doiron-Leyraud, N., Hassinger, E., Daou, R., Rondeau, M., Ramshaw, B., Liang, R., Bonn, D., Hardy, W., Pyon, S., Takayama, T., Takagi, H., Sheikin, I., Malone, L., Proust, C., Behnia, K., and Taillefer, L. **2**, 432 August (2011).

[3] Hücker, M., Christensen, N. B., Holmes, A. T., Blackburn, E., Forgan, E. M., Liang, R., Bonn, D. A., Hardy, W. N., Gutowski, O., Zimmermann, M. v., Hayden, S. M., and Chang, J. *Phys. Rev. B* **90**, 054514 Aug (2014).

[4] Croft, T. P., Lester, C., Senn, M. S., Bombardi, A., and Hayden, S. M. *Phys. Rev. B* **89**, 224513 Jun (2014).

[5] Bednorz, J. G. and Müller, K. A. *Zeitschrift für Physik B Condensed Matter* **64**, 189–193 (1986).

[6] Wu, M. K., Ashburn, J. R., Torng, C. J., Hor, P. H., Meng, R. L., Gao, L., Huang, Z. J., Wang, Y. Q., and Chu, C. W. *Phys. Rev. Lett.* **58**, 908–910 Mar (1987).

[7] Schilling, A., Cantoni, M., Guo, J. D., and Ott, H. R. *Nature* **363**, 56–58 May (1993).

[8] Drozdov, A. P., Eremets, M. I., Troyan, I. A., Ksenofontov, V., and Shylin, S. I. *Nature* **525**, 73–76 September (2015).

[9] Hawthorn, D. G. *Thermal conduction in the high temperature superconductors LSCO and TL2201: A field and doping dependent study*. PhD thesis, University of Toronto, (2005).

[10] Benhabib, S. *Vie et mort du Pseudogap dans l'état normal du cuprate* $Bi_2Sr_2CaCu_2O_{8+\alpha}$. PhD thesis, Physique Ile-de-France Laboratoire Matériaux et Phénomènes Quantiques, (2016).

[11] Broun, D. M. *Nat Phys* **4**, 170–172 March (2008).

[12] Keimer, B., Belk, N., Birgeneau, R. J., Cassanho, A., Chen, C. Y., Greven, M., Kastner, M. A., Aharony, A., Endoh, Y., Erwin, R. W., and Shirane, G. *Phys. Rev. B* **46**, 14034–14053 December (1992).

[13] Nakamae, S., Behnia, K., Mangkorntong, N., Nohara, M., Takagi, H., Yates, S. J. C., and Hussey, N. E. *Phys. Rev. B* **68**, 100502 September (2003).

[14] Kimura, H., Hirota, K., Matsushita, H., Yamada, K., Endoh, Y., Lee, S.-H., Majkrzak, C. F., Erwin, R., Shirane, G., Greven, M., Lee, Y. S., Kastner, M. A., and Birgeneau, R. J. *Phys. Rev. B* **59**, 6517–6523 March (1999).

[15] Wakimoto, S., Shirane, G., Endoh, Y., Hirota, K., Ueki, S., Yamada, K., Birgeneau, R. J., Kastner, M. A., Lee, Y. S., Gehring, P. M., and Lee, S. H. *Phys. Rev. B* **60**, R769–R772 July (1999).

[16] Lake, B., Ronnow, H. M., Christensen, N. B., Aeppli, G., Lefmann, K., McMorrow, D. F., Vorderwisch, P., Smeibidl, P., Mangkorntong, N., Sasagawa, T., Nohara, M., Takagi, H., and Mason, T. E. *Nature* **415**, 299–302 January (2002).

[17] Chang, J., Niedermayer, C., Gilardi, R., Christensen, N. B., Rønnow, H. M., McMorrow, D. F., Ay, M., Stahn, J., Sobolev, O., Hiess, A., Pailhes, S., Baines, C., Momono, N., Oda, M., Ido, M., and Mesot, J. *Phys. Rev. B* **78**, 104525 September (2008).

[18] Kofu, M., Lee, S.-H., Fujita, M., Kang, H.-J., Eisaki, H., and Yamada, K. *Phys. Rev. Lett.* **102**, 047001 January (2009).

[19] Julien, M.-H. *Physica B: Condensed Matter* **329**, 693–696 (2003).

[20] Chang, J., Blackburn, E., Holmes, A. T., Christensen, N. B., Larsen, J., Mesot, J., Liang, R., Bonn, D. A., Hardy, W. N., Watenphul, A., Zimmermann, M. v., Forgan, E. M., and Hayden, S. M. *Nat Phys* **8**, 871–876 December (2012).

[21] Kawasaki, S., Lin, C., Kuhns, P. L., Reyes, A. P., and Zheng, G.-q. *Phys. Rev. Lett.* **105**, 137002 September (2010).

[22] Yamada, K., Lee, C. H., Kurahashi, K., Wada, J., Wakimoto, S., Ueki, S., Kimura, H., Endoh, Y., Hosoya, S., Shirane, G., Birgeneau, R. J., Greven, M., Kastner, M. A., and Kim, Y. J. *Phys. Rev. B* **57**, 6165–6172 March (1998).

[23] Platé, M., Mottershead, J. D. F., Elfimov, I. S., Peets, D. C., Liang, R., Bonn, D. A., Hardy, W. N., Chiuzbaian, S., Falub, M., Shi, M., Patthey, L., and Damascelli, A. *Phys. Rev. Lett.* **95**, 077001 August (2005).

[24] Vignolle, B., Carrington, A., Cooper, R. A., French, M. M. J., Mackenzie, A. P., Jaudet, C., Vignolles, D., Proust, C., and Hussey, N. E. *Nature* **455**, 952–955 October (2008).

[25] Hossain, M. A., Mottershead, J. D. F., Fournier, D., Bostwick, A., McChesney, J. L., Rotenberg, E., Liang, R., Hardy, W. N., Sawatzky, G. A., Elfimov, I. S., Bonn, D. A., and Damascelli, A. *Nature Physics* **4**, 527 June (2008).

[26] Doiron-Leyraud, N., Proust, C., LeBoeuf, D., Levallois, J., Bonnemaison, J.-B., Liang, R., Bonn, D. A., Hardy, W. N., and Taillefer, L. *Nature* **447**, 565–568 May (2007).

[27] Badoux, S., Tabis, W., Laliberté, F., Grissonnanche, G., Vignolle, B., Vignolles, D., Béard, J., Bonn, D. A., Hardy, W. N., Liang, R., Doiron-Leyraud, N., Taillefer, L., and Proust, C. *Nature* **531**, 210–214 March (2016).

[28] Mackenzie, A. P., Julian, S. R., Sinclair, D. C., and Lin, C. T. *Phys. Rev. B* **53**, 5848–5855 March (1996).

[29] Collignon, C., Badoux, S., Afshar, S. A. A., Michon, B., Laliberté, F., Cyr-Choinière, O., Zhou, J.-S., Licciardello, S., Wiedmann, S., Doiron-Leyraud, N., and Taillefer, L. *Phys. Rev. B* **95**, 224517 June (2017).

[30] Barisic, N., Badoux, S., Chan, M. K., Dorow, C., Tabis, W., Vignolle, B., Yu, G., Beard, J., Zhao, X., Proust, C., and Greven, M. *Nat Phys* **9**, 761–764 December (2013).

[31] Segawa, K. and Ando, Y. *Phys. Rev. B* **69**, 104521 March (2004).

[32] Ando, Y., Kurita, Y., Komiya, S., Ono, S., and Segawa, K. *Phys. Rev. Lett.* **92**, 197001 May (2004).

[33] Doiron-Leyraud, N., Lepault, S., Cyr-Choinière, O., Vignolle, B., Grissonnanche, G., Laliberté, F., Chang, J., Barišić, N., Chan, M. K., Ji, L., Zhao, X., Li, Y., Greven, M., Proust, C., and Taillefer, L. *Phys. Rev. X* **3**, 021019 June (2013).

[34] Noda, T., Eisaki, H., and Uchida, S.-i. *Science* **286**, 265 October (1999).

[35] Adachi, T., Noji, T., and Koike, Y. *Phys. Rev. B* **64**, 144524 September (2001).

[36] Suzuki, T., Goto, T., Chiba, K., Minami, M., Oshima, Y., Fukase, T., Fujita, M., and Yamada, K. *Phys. Rev. B* **66**, 104528 September (2002).

[37] Behnia, K., Jaccard, D., and Flouquet, J. *Journal of Physics: Condensed Matter* **16**, 5187 (2004).

[38] Jaudet, C., Vignolles, D., Audouard, A., Levallois, J., LeBoeuf, D., Doiron-Leyraud, N., Vignolle, B., Nardone, M., Zitouni, A., Liang, R., Bonn, D. A., Hardy, W. N., Taillefer, L., and Proust, C. *Phys. Rev. Lett.* **100**, 187005 May (2008).

[39] Taillefer, L. *Journal of Physics: Condensed Matter* **21**, 164212 (2009).

[40] Grissonnanche, G., Cyr-Choinière, O., Laliberté, F., René de Cotret, S., Juneau-Fecteau, A., Dufour-Beauséjour, S., Delage, M. , LeBoeuf, D., Chang, J., Ramshaw, B. J., Bonn, D. A., Hardy, W. N., Liang, R., Adachi, S., Hussey, N. E., Vignolle, B., Proust, C., Sutherland, M., Krämer, S., Park, J. H., Graf, D., Doiron-Leyraud, N., and Taillefer, L. *Nat Commun* **5**, 1–8 February (2014).

[41] Blanco-Canosa, S., Frano, A., Schierle, E., Porras, J., Loew, T., Minola, M., Bluschke, M., Weschke, E., Keimer, B., and Le Tacon, M. *Phys. Rev. B* **90**, 054513 August (2014).

[42] Harrison, N. and Sebastian, S. E. *New Journal of Physics* **14**, 095023 (2012).

[43] Cooper, R. A., Wang, Y., Vignolle, B., Lipscombe, O. J., Hayden, S. M., Tanabe, Y., Adachi, T., Koike, Y., Nohara, M., Takagi, H., Proust, C., and Hussey, N. E. *Science* **323**, 603 January (2009).

[44] Christensen, N. B., Chang, J., Larsen, J., Fujita, M., Oda, M., Ido, M., Momono, N., Forgan, E. M., Holmes, A. T., Mesot, J., Huecker, M., and Zimmermann, M. v. *ArXiv e-prints* April (2014).

[45] Grissonnanche, G. *Une fable de phases en interaction dans les cuprates supraconducteurs contar le transport thermique*. PhD thesis, Université of Sherbrooke, March (2016).

[46] Behnia, K. *Journal of Physics: Condensed Matter* **21**, 113101 (2009).

[47] White, G. K. and Meeson, P. *Experimental Techniques in Low-Temperature Physics*. 9780198514275. Oxford University Press, forth edition, April (2002).

[48] Inyushkin, A. V.; Leicht, K. E. P. *Cryogenics* **38**, 299–304 (1998).

[49] Badoux, S., Afshar, S., Michon, B., Ouellet, A., Fortier, S., LeBoeuf, D., Croft, T., Lester, C., Hayden, S., Takagi, H., Yamada, K., Graf, D., Doiron-Leyraud, N., and Taillefer, L. *Phys. Rev. X* **6**, 021004 April (2016).

[50] Balakirev, F. F., Betts, J. B., Migliori, A., Tsukada, I., Ando, Y., and Boebinger, G. S. *Phys. Rev. Lett.* **102**, 017004 January (2009).

[51] Boebinger, G. S., Ando, Y., Passner, A., Kimura, T., Okuya, M., Shimoyama, J., Kishio, K., Tamasaku, K., Ichikawa, N., and Uchida, S. *Phys. Rev. Lett.* **77**, 5417–5420 December (1996).

[52] Chang, J., Daou, R., Proust, C., LeBoeuf, D., Doiron-Leyraud, N., Laliberté, F., Pingault, B., Ramshaw, B. J., Liang, R., Bonn, D. A., Hardy, W. N., Takagi, H., Antunes, A. B., Sheikin, I., Behnia, K., and Taillefer, L. *Phys. Rev. Lett.* **104**, 057005 February (2010).

[53] Chang, J. and Ivashko, O. April (2018).

[54] Christensen, N. B., Chang, J., Larsen, J., Fujita, M., Oda, M., Ido, M., Momono, N., Forgan, E. M., Holmes, A. T., Mesot, J., Huecker, M., and Zimmermann, M. v. *ArXiv e-prints* April (2014).

[55] Haug, D., Hinkov, V., Sidis, Y., Bourges, P., Christensen, N. B., Ivanov, A., Keller, T., Lin, C. T., and Keimer, B. *New Journal of Physics* **12**, 105006 (2010).

[56] LeBoeuf, D., Doiron-Leyraud, N., Vignolle, B., Sutherland, M., Ramshaw, B. J., Levallois, J., Daou, R., Laliberté, F., Cyr-Choinière, O., Chang, J., Jo, Y. J., Balicas, L., Liang, R., Bonn, D. A., Hardy, W. N., Proust, C., and Taillefer, L. *Phys. Rev. B* **83**, 054506 February (2011).

[57] Efetov, K. B., Meier, H., and Pepin, C. *Nat Phys* **9**, 442–446 July (2013).

[58] Laliberté, F. Master's thesis, Université de Sherbrooke, October (2010).